Chapter 2

TRMM Latent Heating Retrieval: Applications and Comparisons with Field Campaigns and Large-Scale Analyses

W.-K. TAO,[a] Y. N. TAKAYABU,[b] S. LANG,[a,c] S. SHIGE,[d] W. OLSON,[a,e] A. HOU,[a] G. SKOFRONICK-JACKSON,[a] X. JIANG,[f,g] C. ZHANG,[h] W. LAU,[i] T. KRISHNAMURTI,[j] D. WALISER,[f] M. GRECU,[a,k] P. E. CIESIELSKI,[l] R. H. JOHNSON,[l] R. HOUZE,[m] R. KAKAR,[n] K. NAKAMURA,[o] S. BRAUN,[l] S. HAGOS,[h] R. OKI,[p] AND A. BHARDWAJ[j]

[a] *Mesoscale Atmospheric Processes Laboratory, NASA Goddard Space Flight Center, Greenbelt, Maryland*
[b] *Atmosphere and Ocean Research Institute, The University of Tokyo, Kashiwa, Chiba, Japan*
[c] *Science Systems and Applications Inc., Lanham, Maryland*
[d] *Division of Earth and Planetary Sciences, Kyoto University, Kyoto, Japan*
[e] *UMBC Joint Center for Earth Systems Technology, University of Maryland at Baltimore, Baltimore, Maryland*
[f] *Jet Propulsion Laboratory, California Institute of Technology, Pasadena, California*
[g] *Joint Institute for Regional Earth System Science and Engineering, University of California, California*
[h] *Rosenstiel School of Marine and Atmospheric Science, University of Miami, Miami, Florida*
[i] *Earth System Science Interdisciplinary Center, Joint Global Change Research Institute, University of Maryland, College Park, College Park, Maryland*
[j] *Department of Meteorology, Florida State University, Tallahassee, Florida*
[k] *Goddard Earth Sciences Technology and Research, Morgan State University, Baltimore, Maryland*
[l] *Department of Atmospheric Science, Colorado State University, Fort Collins, Colorado*
[m] *Department of Atmospheric Science, University of Washington, Seattle, Washington*
[n] *NASA Headquarters, Science Mission Directorate, Washington, D.C.*
[o] *Hydrospheric Atmospheric Research Center, Nagoya University, Nagoya, Japan*
[p] *Earth Observation Research Center, Japan Aerospace Exploration Agency, Tsukuba, Japan*

ABSTRACT

Yanai and coauthors utilized the meteorological data collected from a sounding network to present a pioneering work in 1973 on thermodynamic budgets, which are referred to as the apparent heat source (Q_1) and apparent moisture sink (Q_2). Latent heating (LH) is one of the most dominant terms in Q_1. Yanai's paper motivated the development of satellite-based LH algorithms and provided a theoretical background for imposing large-scale advective forcing into cloud-resolving models (CRMs). These CRM-simulated LH and Q_1 data have been used to generate the look-up tables in Tropical Rainfall Measuring Mission (TRMM) LH algorithms. A set of algorithms developed for retrieving LH profiles from TRMM-based rainfall profiles is described and evaluated, including details concerning their intrinsic space–time resolutions. Included in the paper are results from a variety of validation analyses that define the uncertainty of the LH profile estimates. Also, examples of how TRMM-retrieved LH profiles have been used to understand the life cycle of the MJO and improve the predictions of global weather and climate models as well as comparisons with large-scale analyses are provided. Areas for further improvement of the TRMM products are discussed.

1. Introduction

Release of latent heat during precipitation formation is of immense consequence to the nature of large- and small-scale atmospheric circulations, particularly in the

Corresponding author address: Dr. Wei-Kuo Tao, NASA/Goddard Space Flight Center, Mesoscale Atmospheric Processes Laboratory (Code 612), Greenbelt, MD 20771.
E-mail: wei-kuo.tao-1@nasa.gov

DOI: 10.1175/AMSMONOGRAPHS-D-15-0013.1

tropics where various large-scale tropical modes dominated by latent heating (LH) persist and vary on a global scale. Latent heat release and its variation are without doubt some of the most important physical processes within the atmosphere and thus play a central role in Earth's water and energy cycle. The launch of the Tropical Rainfall Measuring Mission satellite (TRMM), a joint U.S.–Japan project, in November 1997 made it possible for quantitative measurements of tropical rainfall to be obtained on a continuous basis over the global tropics. TRMM has provided much-needed accurate measurements of rainfall as well as estimates of the four-dimensional structure of LH over the global tropics. Over the last few years, standard LH products from TRMM measurements have become established as a valuable resource for scientific research and applications [see a review by Tao et al. (2006) and the papers published in the *Journal of Climate* special collection on TRMM diabatic heating]. Such products enable new insights and investigations into the complexities of convective system life cycles, diabatic heating controls and feedbacks related to mesoscale and synoptic-scale circulations and their prediction, the relationship of tropical patterns of LH to the global circulation and climate, and strategies for improving cloud parameterizations in environmental prediction models. TRMM's success provided the impetus for another major international satellite mission known as the Global Precipitation Measurement (GPM), launched by NASA and JAXA in February 2014 (http://gpm.nasa.gov). As the centerpiece of NASA's Weather and Global Water/Energy Cycle research programs, GPM consists of a constellation of satellites provided by a consortium of international partners to provide the next generation of spaceborne precipitation measurements with better sampling (3-hourly over a specific location), higher accuracy (with a Ku-Ka band radar), finer spatial resolution (up to $0.1° \times 0.1°$), and greater coverage (from the tropics to high latitudes) relative to TRMM.

LH is dominated by phase changes between water vapor and small liquid or frozen cloud-sized particles. It consists of the condensation of cloud droplets; evaporation of cloud droplets and raindrops; freezing of cloud droplets and raindrops; melting of ice, snow, and graupel/hail; and the deposition and sublimation of ice particles. It is important to keep in mind that eddy heat flux convergence from cloud motions can also redistribute the heating or cooling associated with LH vertically and horizontally. LH cannot be measured directly with current techniques, including current remote sensing or in situ instruments, which explains why nearly all satellite retrieval schemes depend heavily on some type of cloud-resolving model (CRM) (Tao et al. 2006).

However, the apparent heat source or Q_1, of which LH is an important component, can be derived indirectly by measuring vertical profiles of temperature and the associated wind fields from extensive rawinsonde networks through a residual method (Yanai et al. 1973). This residual approach was first described in seminal papers by Professor Yanai (Yanai 1961; Yanai et al. 1973) and expressed by

$$Q_1 = \overline{\pi}\left[\frac{\partial\overline{\theta}}{\partial t} + \overline{\mathbf{V}}\cdot\nabla\overline{\theta} + \overline{w}\,\frac{\partial\overline{\theta}}{\partial z}\right], \tag{2-1}$$

where $\overline{\pi}$ is the nondimensional pressure, $\mathbf{V}$ is the horizontal wind vector, and the overbars denote large-scale horizontal averages. The right-hand side (RHS) is the total derivative of θ, the potential temperature, (times the nondimensional pressure) measurable from radiosonde data. Here the large-scale vertical motion w is diagnosed from the horizontal winds via the kinematic method with appropriate boundary conditions on w at the surface and the tropopause. There is an accompanying equation for the apparent moisture sink or drying (Q_2), which is similar to Eq. (2-1) except that $\overline{\theta}$ is replaced by water vapor specific humidity ($\overline{q}$) and Q_1 is replaced by negative Q_2. To derive Eq. (2-1), Yanai et al. (1973) stated that "we consider an ensemble of cumulus clouds, which is embedded in a tropical large-scale motion system, then we imagine a horizontal area that is large enough to contain the ensemble of clouds, but small enough to be regarded as a fraction of the large-scale system."

Both the vertical velocity in the third term on the RHS and the horizontal and vertical advection terms on the RHS of Eq. (2-1) have been used to force CRMs (or cumulus ensemble models) to study the response of convective systems to large and mesoscale processes (Soong and Tao 1980). This CRM approach to studying cloud and precipitation processes is called *cloud ensemble modeling* [Soong and Tao 1980; Tao and Soong 1986; Tao et al. 1987; Krueger 1988; Moncrieff et al. 1997; also see review papers by Tao (2003, 2007) and Tao and Moncrieff (2009)]. It allows many clouds of various sizes and stages to exist at any given time. The advantage is that modeled rainfall Q_1 and Q_2 usually agree well with observations (Tao 2003; Randall et al. 2003; and others). The model results also include cloud statistics representing different types of cloud systems over their life cycle. Large-scale forcing derived from many field programs (e.g., GATE, TOGA COARE, SCSMEX, TWP-ICE, and others; see the appendix for expansions used in this chapter) have been used to drive CRMs. These CRM-simulated datasets are especially valuable for LH algorithm developers (see Tao et al. 1990, 1993, 2000, 2006, 2010; Shige et al. 2004, 2007, 2008, 2009; Grecu and Olson 2006).

The Madden–Julian oscillation (MJO) is one of the most prominent climate variability modes and exerts

pronounced influences on global climate and weather systems (e.g., Zhang 2005; Lau and Waliser 2011). Current general circulation models (GCMs), however, exhibit rather limited capability in representing the MJO (e.g., Slingo et al. 2005; Lin et al. 2006; Kim et al. 2009). Meanwhile, the fundamental physics of the MJO are still elusive. The essential roles of various diabatic heating components for the MJO have been suggested based on GCM studies, including shallow convective heating (e.g., Zhang and Mu 2005; Benedict and Randall 2009; Li et al. 2009; Zhang and Song 2009), stratiform heating (e.g., Fu and Wang 2009; Seo and Wang 2010), and radiative heating (e.g., Lee et al. 2001; Raymond 2001; Sobel and Gildor 2003). A transition in the vertical heating structure during MJO evolution—namely, from shallow to deep, and then to stratiform—has been reported based on TOGA COARE observations (Lin et al. 2004; Kiladis et al. 2005). However, this vertical tilting structure in the MJO heating field was not clearly evident in sounding observations during the Mirai Indian Ocean Cruise for the Study of the MJO Convection Onset (MISMO; Katsumata et al. 2009), as well as in a composite study over both the Indian and western Pacific Oceans (Morita et al. 2006) and in a case study over the Indian Ocean during the 1998/99 winter (Jiang et al. 2009) based on earlier versions of TRMM heating estimates. A comprehensive characterization of the vertical heating structure of the MJO would be of considerable value in elucidating its essential physics.

This paper describes the second major goal of TRMM of obtaining credible LH estimates as well as their applications within TRMM's zone of coverage, the standard TRMM LH products, and areas for further improvement. Section 2 describes CRM-simulated heating structure estimates in comparison with diagnostic Q_1 estimates based on observed radiosonde profiles of wind, pressure, and temperature. Section 3 gives an overview of the five LH retrieval algorithms developed for TRMM applications while section 4 details the relevant field campaigns used in their development as well as efforts by algorithm developers to validate their LH algorithms. Section 5 highlights applications of the LH products including comparisons with large-scale reanalyses regarding the life cycle of the MJO and improving monsoon forecasts and the physics of global models. Finally, the conclusions as well as final remarks intended to stimulate further research are given in section 6.

2. Relating quantitative cloud heating estimates to CRMs

CRMs are one of the most important tools used to establish quantitative relationships between diabatic heating and rainfall. This is because LH is dominated by phase changes between water vapor and small, cloud-sized particles; these particles as well as their changes are difficult to detect directly using remote sensing techniques (although some passive microwave frequencies respond to path-integrated cloud water and *CloudSat* can detect such particles in the tops of clouds). CRMs, however, employing sophisticated microphysical schemes (that are by no means yet perfect) can explicitly simulate the conversion of cloud condensate into raindrops and various forms of precipitating ice. It is these different forms of precipitation that are most readily detected from space, and which ultimately reach the surface in the form of rain in the tropics. CRMs have been used for TRMM for both rainfall and heating retrieval algorithm development.

Under the Boussinesq approximation, the heat (temperature) budget can be explicitly calculated by a CRM (e.g., Tao and Simpson 1989):

$$Q_1 - Q_R = \overline{\pi}[-(1/\overline{\rho})(\overline{\partial \overline{\rho} w' \theta'/\partial z}) - \overline{\nabla \cdot V' \theta'}] + (1/c_p)[L_v(c-e) + L_f(f-m) + L_s(d-s)], \quad (2\text{-}2)$$

where the primes indicate deviations from the large-scale environment due to smaller-scale cloud processes. The variable θ is potential temperature, $\overline{\rho}$ is density, $\overline{\pi} = (p/p_{00})^{R/c_p}$ is nondimensional pressure (where p and p_{00} are dimensional and reference pressures, respectively, with p_{00} taken as 1000 hPa), and c_p and R are the specific heat of dry air at constant pressure and the gas constant of dry air, respectively. The variables L_v, L_f, and L_s are the latent heats of condensation, freezing, and sublimation, respectively, while the variables c, e, f, m, d, and s are the condensation of cloud droplets; evaporation of cloud droplets and rain drops; freezing of water droplets and rain drops; melting of ice crystals, snowflakes, graupel, and hail; deposition of ice crystals; and sublimation of all ice hydrometeors, respectively. The quantity $(1/c_p)[L_v(c-e) + L_f(f-m) + L_s(d-s)]$ is defined as the LH due to microphysical phase changes while the first two terms on the RHS of Eq. (2-2) are the vertical and horizontal eddy heat flux divergence, respectively. The horizontal divergence term is neglected when Eq. (2-2) is spatially averaged over an area suitable for diagnostic analysis.

Figure 2-1 shows CRM-simulated time-domain mean profiles of heating/cooling due to the individual microphysical processes (i.e., condensation, evaporation, deposition, sublimation, melting, and freezing) in the convective and stratiform regions of a tropical MCS using the Goddard Cumulus Ensemble model (GCE;

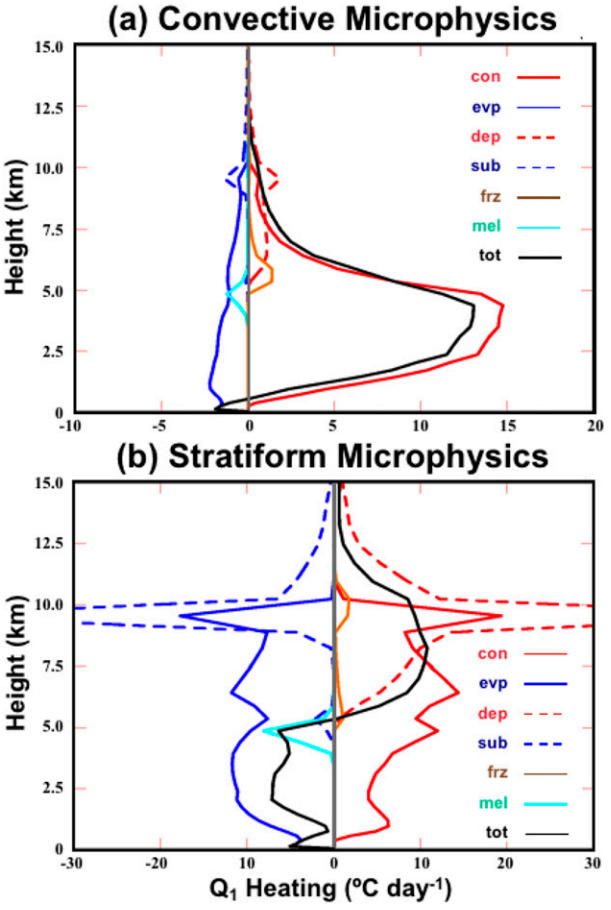

FIG. 2-1. Goddard Cumulus Ensemble model (GCE)-simulated time-mean profiles of LH components averaged over the (a) convective and (b) stratiform region. The components consist of condensation (solid red), evaporation (solid blue), deposition (dashed red), sublimation (dashed blue), freezing (solid orange), melting (solid turquoise), and total (solid black).

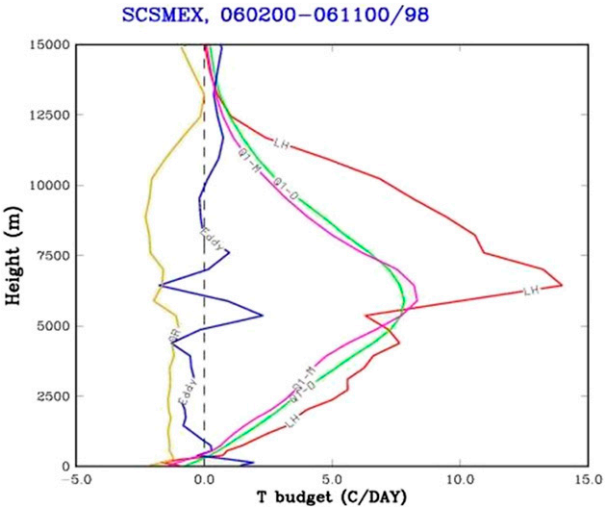

FIG. 2-2. GCE-simulated time-domain-mean profiles of net condensation or LH ($c - e + d - s + f - m$, red), eddy heat flux divergence (blue), Q_R (yellow), and Q_1 (purple). The observed Q_1 (green) estimated from a sounding network is also shown for comparison. Adapted from Tao (2007).

Tao and Simpson 1993). Condensation and evaporation have the largest magnitudes in the convective region with evaporation and sublimation about one-third the values of the condensation and deposition rates, respectively. Melting and freezing are small compared to condensation, evaporation, deposition, and sublimation; however, melting is responsible for converting precipitating ice to rain, which can then fall to the surface. Figure 2-2 shows vertical profiles of LH, vertical eddy heat flux divergence, radiation, and Q_1 averaged over a 9-day period during SCSMEX over the northern enhanced sounding array (NESA). LH is the largest term in the Q_1 budget via the heat released by condensation and deposition (as shown in Fig. 2-1). Its peak is around 6.5 km. The radiative term (Q_R) accounts for about 1°–3° of cooling per day. The eddy transport is the smallest term, but it does redistribute heat through cloud updrafts and downdrafts. The CRM-simulated Q_1 profile is in very good agreement with the observed [i.e., Fig. 3 in Tao (2007)].

3. Overview of the TRMM LH retrieval algorithms

The primary TRMM instruments used to measure rainfall are the TRMM Microwave Imager (TMI), Precipitation Radar (PR), and the Visible and Infrared Scanner (VIRS; Kummerow et al. 1998; for additional details see http://trmm.gsfc.nasa.gov). Five different TRMM LH algorithms designed for applications with satellite-estimated surface rain rate and precipitation profile inputs have been developed, compared, validated, and applied in the past decade [see a review by Tao et al. (2006)]. They are the 1) Goddard convective–stratiform heating (CSH) algorithm, 2) spectral latent heating (SLH) algorithm, 3) Goddard TRAIN (Trained Radiometer) algorithm, 4) hydrometeor heating (HH) algorithm, and 5) precipitation radar heating (PRH) algorithm. CRM-simulated vertical heating profiles are required in the form of look-up tables (LUTs) for the CSH, SLH, and TRAIN heating algorithms. CRM-simulated rainfall and vertical heating structures are also used for these heating algorithms for validation via consistency checks. Neither the HH nor the PRH algorithm uses precalculated LH profiles in LUTs. Instead, both schemes estimate the net flux of water mass into (out of) layers and assume that under steady-state conditions net fluxes are compensated for by a local decrease (increase) of hydrometeors by microphysical processes. Thus, a decrease in mass is associated with

TABLE 2-1. Summary of the five LH algorithms [see Tao et al. (2006) for further details and salient references]. Data inputs, retrieved products, and salient references are included. The conventional relationship between Q_1 (apparent heat source), LH, and Q_R (radiative heating) is expressed by $Q_1 - Q_R$ = LH + EHT, where the final term represents eddy heat transport by clouds (vertically integrated EHT is zero; i.e., it provides no explicit influence on surface rainfall). TMI is the TRMM Microwave Imager and PR the TRMM Precipitation Radar.

	Required TRMM data	Algorithm products	Key references in algorithm description	Algorithm developers
CSH (convective-stratiform heating)	PR, TMI, PR-TMI	Q_1, LH, Q_2	Tao et al. (1990, 1993, 2000, 2001, 2010)	W.-K. Tao and S. E. Lang
SLH (spectral latent heating)	PR	LH, $Q_1 - Q_R$ Q_2	Shige et al. (2004, 2007, 2008, 2009)	S. Shige and Y. N. Takayabu
TRAIN (trained radiometer algorithm)	TMI (PR training)	$Q_1 - Q_R$, LH	Grecu and Olson (2006), Olson et al. (2006) Grecu et al. (2009)	M. Grecu and W. Olson
HH (hydrometeor heating)	PR-TMI	LH	Yang and Smith (1999b), Yang et al. (2006)	E. A. Smith and Y. Song
PRH (precipitation radar heating)	PR	LH	Satoh and Noda (2001)	S. Satoh and A. Noda

evaporation, melting, or sublimation cooling, whereas an increase is associated with condensation, freezing, or deposition heating. The overall strengths and weaknesses of these five different heating algorithms are shown in Table 2 of Tao et al. (2006).

Table 2-1 gives a summary of the five algorithms, including the type(s) of TRMM input data used to generate their associated heating product(s), the type of heating product(s) produced, and the salient reference(s) describing their design. Additional improvements made to the SLH, TRAIN, and CSH algorithms as well as brief descriptions of the HH and PRH algorithms are presented next.

a. The CSH algorithm

Diagnostic budget studies (e.g., Houze 1982; Johnson 1984) and cloud modeling studies [see review by Tao (2003)] have shown that characteristic LH profiles in the stratiform regions of tropical MCSs are considerably different than the characteristic LH profiles in the convective regions. In general, for both observed and simulated convective systems, evaporative cooling in the lower troposphere below a bow-shaped positive heating profile in the middle and upper cloud layers (peaking in the middle to upper troposphere) is the dominant feature within stratiform precipitation regions (i.e., the archetypical reverse S-shaped stratiform LH profile), while a combination of vertically continuous condensation and deposition heating (peaking in the middle troposphere) is the dominant signature for convective rain areas (i.e., the archetypical, deep, all-positive, bow-shaped convective LH profile). Based on these findings, the CSH algorithm was developed and described by Tao et al. (1993).

Recently, the CSH algorithm was redesigned and improved (Tao et al. 2010). The key difference between the new and old versions (Tao et al. 1993, 2000, 2001) involves the new LUTs[1] and how they are accessed. First, there are many more heating profiles (approximately 700 total compared to 20 in the previous version[2]) in the new LUTs due to their being separated into detailed intensity and stratiform bins. And second, the profiles are distributed and thus accessed according to conditional rain rates. Together these lead to several potential advantages regarding heating structure. Obviously, having many more profiles in the LUTs allows for the possibility of having many more heating structures. For example, rather than just having shallow (i.e., <5 km) or deep heating profiles, the new LUTs allow the depth of heating to vary considerably.[3] Using conditional rain rates is what allows those structures to be better differentiated. For example, given a stratiform fraction and an average rain rate over a region (i.e., a 0.5° × 0.5° area), knowing that average rain rate is due to a small area of intense rain (e.g., a single intense convective cell) rather than a larger area of weak rain (e.g., a broader field of weaker convective cells) allows the algorithm to select a more representative heating

[1] To date, field program data that have been examined in conjunction with the CSH algorithm include 1) GATE, 2) EMEX, 3) PRE-STORM, 4) TOGA COARE, 5) SCSMEX, 6) TRMM-LBA, 7) KWAJEX, and 8) DOE-ARM.

[2] These profiles were obtained by distributing heating/cooling profiles from model subdomains (64 km or the approximate grid size of the TRMM rain retrievals) into the same conditional rain intensity and stratiform percentage bins used to differentiate the surface rainfall distributions. Separate LUTs were constructed for each of the three main components: latent, eddy (horizontal and vertical combined), and radiative.

[3] Mean echo-top heights from the PR and from the model correlate nicely over almost the entire range of LUT bins (not shown).

structure. In the older version, these two rain areas would have been treated the same. The newer LUTs include CRM-generated LH, eddy heating, and radiative heating/cooling at common levels on a common grid. They can thus easily provide the eddy and radiative terms to other LH algorithm groups[4] (at the same rainfall intensity and stratiform percentage).

b. The SLH algorithm

Spectral representation of precipitation profiles obtained from the PR algorithm by use of a small set of distinct profile properties, as reported by Takayabu (2002), provide the basis for the SLH algorithm, which was introduced and modified by Shige et al. (2004, 2007, 2008, 2009). This algorithm is currently intended for use with PR-retrieved rain rate profiles only and estimates LH, $Q_1 - Q_R$, and Q_2. Akin to the CSH algorithm, a set of three LUTs is produced using the GCE associated with three types of rainfall: 1) convective, 2) shallow-stratiform, and 3) anvil. Specifically, however, the LUTs are indexed according to vertical rain profile information: precipitation top height (PTH) for convective and shallow stratiform rain and melting-level rain intensity for anvil (deep stratiform with a PTH higher than the melting level) rain. The nomenclature ''spectral'' stems from the spectrally indexed table, designed to reduce the dependency on GCE/CRM simulations from specific field campaigns.

In the latest version of the SLH algorithm, deep stratiform rain is further divided into two new categories: deep stratiform with decreasing precipitation from the melting level toward the surface and deep stratiform with increasing precipitation from the melting level toward the surface (Shige et al. 2013). It computes deep stratiform cooling magnitudes as a function of Pm (melting level) − Ps (surface rain rate), assuming the evaporative cooling rate below the melting level in deep stratiform regions is proportional to the reduction in the precipitation profile toward the surface from the melting level (based on 1D water substance conservation). However, increasing precipitation profiles are found in some portions of stratiform regions, especially in regions adjacent to convective regions where 1D water substance conservation may be invalid. An LUT[5] for deep stratiform with increasing precipitation toward the surface from the melting level is produced with the amplitude determined by Ps.

c. The TRAIN algorithm

The TRAIN heating algorithm is designed specifically for application with TMI passive microwave (PMW) radiance observations. First, precipitation and heating profiles are derived from PR reflectivity profiles, using a method similar to that of Shige et al. (2004), over a one-month span of PR observations. In this method, month-long CRM (i.e., GCE) simulations of precipitation/heating during SCSMEX (18 May–17 June 1998), TOGA COARE (19 December 1992–18 January 1993), and KWAJEX (6 August–5 September 1999) are used to relate vertical reflectivity structure and surface rain rate to vertical heating structure. Since TMI-observed microwave brightness temperatures (Tb) are collocated with PR observations over the PR swath, TMI Tb are assigned to each precipitation/heating profile in the large PR-derived database. The database then serves as a kind of LUT to be used in a Bayesian method to estimate precipitation and LH from the TMI. Given a set of TMI-observed Tb, an estimated precipitation/heating profile is constructed by compositing database precipitation/heating profiles associated with Tb values that are consistent with the TMI-observed Tb values and their uncertainties.

Originally developed for application with SSM/I data, the Bayesian method was adapted for application with TMI radiances and integrated within the GPROF TMI precipitation retrieval algorithm (see Olson et al. 1999, 2006). Versions of the GPROF heating algorithm were used by Rodgers et al. (1998, 2000) to diagnose the relationship between LH distributions and storm intensification within Hurricane Opal and Supertyphoon Paka. More recently, Grecu and Olson (2006) and Grecu et al. (2009) demonstrated that Q_1 profiles from TRAIN were consistent with independent estimates derived from SCSMEX and MISMO rawinsonde analyses. Note that Q_1 was estimated by combining TRAIN estimates of $Q_1 - Q_R$ with Q_R estimates from the Hydrologic Cycle and Earth Radiation Budget (HERB) algorithm of L'Ecuyer and Stephens (2003, 2007).

d. The HH algorithm

The HH algorithm, including its verification and global application, is described in Yang and Smith (1999a,b, 2000). These studies describe how cloud-scale vertical velocity can be estimated using multiple-linear regression based on hydrometeor profile densities as independent input variables. For applications with TRMM level-2 retrievals, the current scheme uses truncated

[4] Since the various algorithms produce different heating, it was recommended by the TRMM Latent Heating Working Group at the Fifth TRMM LH workshop (Annapolis, MD, 27–28 Aug 2007) that CSH should be used to provide the eddy and radiative terms to the other algorithms.

[5] It is based on four 9-day (10–18 Dec 1992, 27 Dec 1992–4 Jan 1993, 9–17 Feb 1993, and 18–26 Feb 1993) and one 8-day (19–26 Dec 1992) TOGA COARE CRM simulation(s).

TABLE 2-2. Location, duration, and references of field campaigns. One of the major objectives of SCSMEX, KWAJEX, and LBA was to provide forcing for CRMs and validation for TRMM LH profiles.

Field experiment	Location	Period	Reference
GATE	Tropical Atlantic	26 Jun–19 Sep 1974	Houze and Betts (1981)
TOGA COARE	Equatorial west Pacific	1 Nov 1992–28 Feb 1993	Webster and Lukas (1992)
SCSMEX (N and S)	South China Sea	2–25 May and 5–22 Jun 1998	Lau et al. (2000)
LBA	Amazonia	1 Nov 1998–28 Feb 1999	Silva Dias et al. (2002)
KWAJEX	Marshall Islands	24 Jul–15 Sep 1999	Yuter et al. (2005)
TWP-ICE	Darwin	21 Jan–12 Feb 2006	May et al. (2008)
MISMO	Equatorial Indian Ocean	24 Oct–25 Nov 2006	Yoneyama et al. (2008)
ARM-SGP-97	Central United States	18 Jun–17 Jul 1997	Ackerman and Stokes (2003)
ARM-SGP-02	Central United States	25 May–15 Jun 2002	Ackerman and Stokes (2003)

Legendre polynomial representations of precipitation mass fluxes from the surface to precipitation top height before taking vertical derivatives, thus preventing retrieval noise from producing unrealistic heating rates. For applications with PR data, no account is made for LH by deposition/sublimation and freezing/melting above and below the melting level since the sensitivity of the PR is only 17 dBZ, which is insufficient for detection of most frozen precipitation, particularly for small and/or less dense graupel particles. For applications with TMI data, terminal velocities of precipitating rain and graupel are calculated assuming that both size spectra are distributed according to a Marshall–Palmer distribution.

e. The PRH algorithm

The PRH algorithm uses PR-based retrievals (precipitation profiles and convective/stratiform rain classification) to estimate the vertical LH structure (Satoh and Noda 2001). It requires an initial-guess vertical velocity profile that is used to evaluate a hydrometeor conservation equation under steady-state conditions. In stratiform regions, the LH profile is derived directly from the hydrometeor conservation equation (similar to the HH algorithm). In convective regions, if a net increase of hydrometeors due to microphysics is inferred from the conservation equation, then the associated LH profile is calculated based upon the vertical motion profile, assuming saturated adiabatic ascent. An iterative method is then used to adjust the original vertical motion profile to ensure that the vertically integrated net heating and surface rain rate are consistent.

4. Field campaigns and validation

As discussed in section 1, advective forcing in temperature and water vapor have been used as forcing for CRMs to simulate cloud and precipitation properties including LH, Q_1, and Q_R for TRMM LH algorithm developers. These simulated LH profiles including their convective and stratiform components and their relationship to precipitation have been used to generate LUTs for LH algorithms. In addition, these simulated data and their associated observed Q_1 have been used for validation. This section briefly describes the GCE simulations, field data used, and validation of LH algorithms.

a. Relevant campaigns and their environment

Table 2-2 shows the location, duration, and references for the various field campaigns used in the study and development TRMM LH algorithms. SCSMEX was conducted in May–June 1998. Two major convective events, prior to and during monsoon onset (18–26 May 1998) and post monsoon onset (2–11 June 1998), were observed. The SCSMEX forcing data were obtained from a variational analysis approach (Zhang and Lin 1997; Zhang et al. 2001) and used to drive the GCE for 44 days starting at 0600 UTC 6 May 1998. TOGA COARE was conducted from November 1992 through February 1993 over the central Pacific. The most intense convection during TOGA COARE occurred in mid and late December 1992, prior to the peak in a westerly wind burst around 1 January 1993. Several major convective events occurred around 11–16 and 20–25 December 1992, mainly due to the low-level large-scale convergence of easterlies and westerlies (Lin and Johnson 1996). For TOGA COARE, the large-scale forcing used in the GCE was derived from the intensive flux array (IFA) sounding network (Ciesielski et al. 2003). GATE was conducted in 1974 over the east Atlantic. Cloud systems (nonsquall clusters, a squall line, and scattered convection) for the period 1–8 September 1974 during phase III of GATE have also been simulated using the GCE (Li et al. 1999; Tao 2003). Large-scale GATE forcings from Sui and Yanai (1986) were used to drive the GCE. The environmental conditions for SCSMEX, TOGA COARE, and GATE can be found in Tao et al. (2004). The TOGA COARE surface flux algorithm (Fairall et al. 1996) was used to calculate sea surface fluxes for these oceanic cases.

TABLE 2-3. CRM-simulated rainfall amount and stratiform percentage (%) for SCSMEX (1998), ARM (1997, 2002), TOGA COARE (1992), and GATE (1974). Adapted from Tao et al. (2010).

Field campaign	Simulated rainfall amount (mm day^{-1})	Stratiform rain percentage (%)	Estimated rainfall amount (mm day^{-1})
SCSMEX (NESA)	12.31	42.6	11.35
ARM (1997)	4.31	41.3	4.32
ARM (2002)	4.85	36.0	4.77
TOGA COARE (1992–93)	7.72	47.6	9.32
GATE (1974)	10.56	41.4	11.38

KWAJEX was sponsored by NASA in cooperation with the U.S. Army Kwajalein Atoll/Kwajalein Missile Range and NOAA and was conducted from 23 July to 15 September 1999. It was designed to obtain an empirical physical characterization of precipitating convective clouds over the tropical ocean and to improve physical assumptions made within the TRMM satellite algorithms. TRMM LBA took place in Amazonia in Brazil and focused on the dynamical, microphysical, electrical, and diabatic heating characteristics of tropical convection in the region. Diagnostic analyses from sounding data for KWAJEX and TRMM LBA are reported in Schumacher et al. (2007). TWP-ICE was a comprehensive observing campaign around Darwin, Australia, to study weather and climate change through improved understanding and modeling of cloud and aerosol processes in tropical cloud systems (May et al. 2008); the large-scale forcing derived from its sounding array was described in Xie et al. (2010). The GCE has been used to study convective systems from LBA (Lang et al. 2007, 2011), TWP-ICE (Zeng et al. 2011, 2013), and KWAJEX (Zeng et al. 2008, 2009a,b, 2011).

The ARM program established the SGP site to observe clouds and precipitation for climate research. The site is centered at 36.6°N, 96.5°W. Two summer field campaigns were conducted at the site in 1997 and 2002 and are referred to here as ARM-SGP-97 and -02. The ARM forcing data were also obtained from the variational analysis approach of Zhang and Lin (1997) and Zhang et al. (2001). Surface fluxes taken from site-wide averages of observed fluxes from the ARM energy balance Bowen ratio (EBBR) stations were imposed into the GCE (Zeng et al. 2007, 2011). The ARM-SGP-97 numerical simulation was started at 2330 UTC 18 June 1997 and lasted for 29 days. The ARM-SGP-02 simulation was started at 2030 UTC 25 May 2002 and lasted for 20 days. For the ARM cases, the surface wind did not interact with the boundary layer.

Table 2-3 shows grid-averaged total rainfall and stratiform rain percentage for each of the GCE-simulated cases used to generate the initial CSH version 2 (Tao et al. 2010) LH LUTs. The oceanic cases have more rainfall than the continental ones. This is due primarily to the fact that the oceanic environments have higher precipitable water contents (i.e., more moisture) than the continental [see Table 1 in Tao et al. (2004)]. That is why the SCSMEX simulation has the largest rainfall amount. Although the TOGA COARE environment is generally moister than that for GATE, it has less rainfall because the model simulation starts in November, which did not have many active convective events. In general, the tropical oceanic cases should have a higher stratiform amount (i.e., 40%–50%) than the midlatitude continental cases. However, the ARM cases also have a large stratiform rain fraction (from 36% to 41%) because they include frontal cases. Houze (1997), Zipser et al. (1981), and Gamache and Houze (1983) estimated that widespread stratiform rain accounted for about 32%–49% of the total rainfall during GATE. The fraction of stratiform rainfall from midlatitude squall lines has been estimated at 29%–43% (Rutledge and Houze 1987; Johnson and Hamilton 1988). The GCE-simulated results are in good agreement with these observations. Figure 2-3 shows the geographic

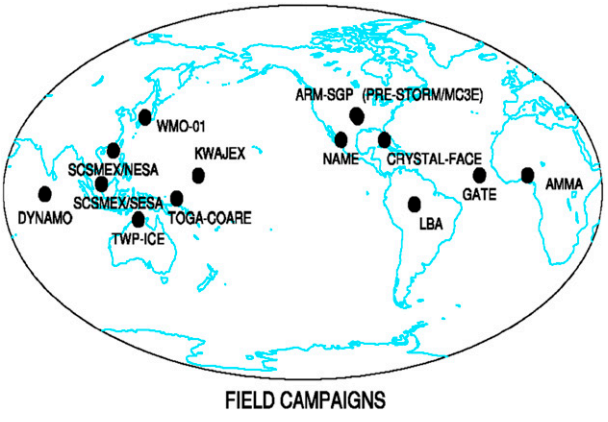

FIG. 2-3. Geographic locations of 12 field campaigns used to provide data to drive and evaluate CRM simulations. These include the ARM-SGP (Southern Great Plains) campaigns conducted in the summer of 1997, the spring of 2000, and the summer of 2002; GATE (1974); KWAJEX (1999); TOGA COARE (conducted in 1992 and 1993); TWP-ICE (2006), SCSMEX/NESA and /SESA (1998), AMMA (2006), MC^{3}E (2011), and AMIE/DYNAMO (2011). MISMO has the same location as DYNAMO. (See the appendix for expansions of acronyms.)

locations of field campaigns used to provide data to drive and evaluate CRM simulations.

b. *Validation of LH algorithms*

Validation of LH profiles retrieved from satellite data is not straightforward because there is no instrument (i.e., no "latent heatometer") or direct means to measure this quantity, and as a result there is no primary calibration standard by which the validation process can be adjudicated. Two methods, consistency checks using CRMs and comparisons with diagnostic budget estimates, have been used for validation.

1) COMPARISON OF CRM HEATING WITH RECONSTRUCTED AND DIAGNOSTIC HEATING

Consistency checks involving CRM-generated heating profiles and both algorithm-reconstructed and diagnostically estimated heating profiles are a useful step in evaluating the performance of a given LH algorithm. In this process, as time-varying CRM-simulated precipitation processes (multiple-day time series) are used to obtain the required input parameters for a given LH algorithm, the algorithm can then be used to reconstruct the actual heating profiles within the CRM simulation using various model quantities (e.g., surface rainfall) as pseudo observations from the model. Finally, both sets of conformal estimates (model and algorithm) can be compared to coincident estimates of diagnostically based heating derived from radiosonde observations. Such observations from various field experiments, as well as simulations of individual precipitation systems, have been used for such consistency checks (Tao et al. 1990, 1993, 2000; Olson et al. 1999, 2006; Shige et al. 2004, 2007, 2008).

It is evident in Fig. 2-4 that the temporal variations of both the CSH- and SLH-reconstructed LH profiles are generally similar to the variations in the GCE simulation profiles.[6] For example, both capture the evolution of a quasi-2-day oscillation, which occurred during the period 1800 UTC 23–1800 UTC 25 December 1992, an oscillation earlier noted by Takayabu et al. (1996). However, as pointed out by Shige et al. (2004), there are noteworthy improvements in the SLH-reconstructed profiles for the shallow-convective stage from 1800 UTC 23 to 0600 UTC 24 December 1992 and in the anvil decay stage from 0600 UTC to 1800 UTC 25 December 1992. Shallow convective heating is more explicitly retrieved by the SLH algorithm because it uses observed

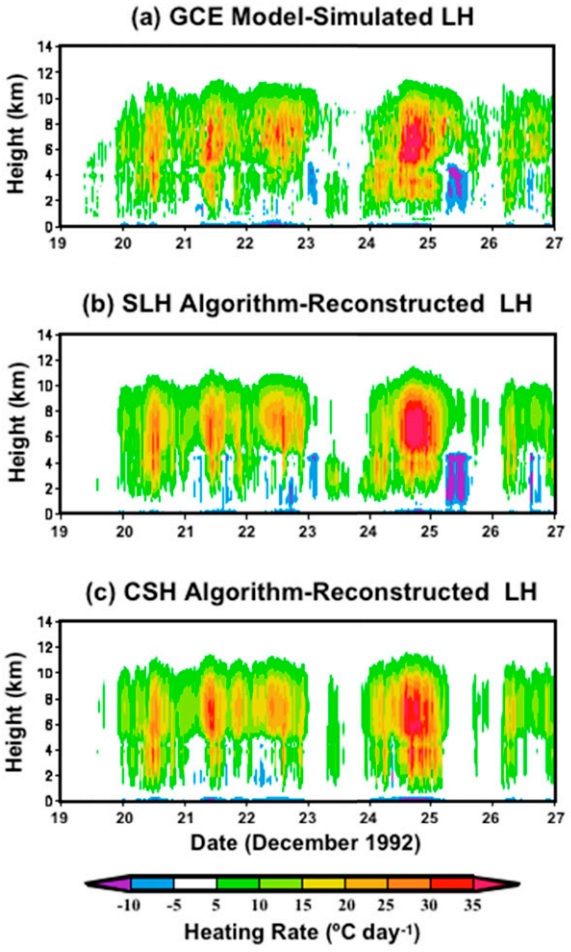

FIG. 2-4. Evolution of LH profiles (5-min intervals) over the TOGA COARE IFA for an 8-day period (19–27 December 1992) from the (a) GCE simulation, (b) SLH algorithm reconstruction, and (c) CSH algorithm reconstruction. The contour interval is 5°C day^{-1}. GCE-simulated convective/shallow–stratiform/anvil stratus fractions, surface rain rates (RRs), PTHs, and melting-level RRs are used as inputs to the SLH algorithm with profiles averaged over a 512-km grid mesh. Adapted from Shige et al. (2004).

information on precipitation depth (i.e., the PTH parameter), and heating profiles in the decaying stage without surface rain (e.g., 1200 UTC 25 December) can be retrieved by the SLH algorithm by using the precipitation rate at the melting level. Both the CSH- and SLH-reconstructed results are smoother than the GCE simulations because the associated LUTs contain averaged profiles for each height/rain bin.

2) COMPARISON OF SATELLITE-RETRIEVED HEATING WITH DIAGNOSTICALLY CALCULATED HEATING

One of the TRMM field campaigns, SCSMEX, which included two sounding networks, the NESA and SESA (northern and southern enhanced sounding array), was

[6] Note that the CSH profiles shown here were from an older version that did not use conditional rain rates like the current version as discussed in section 3a.

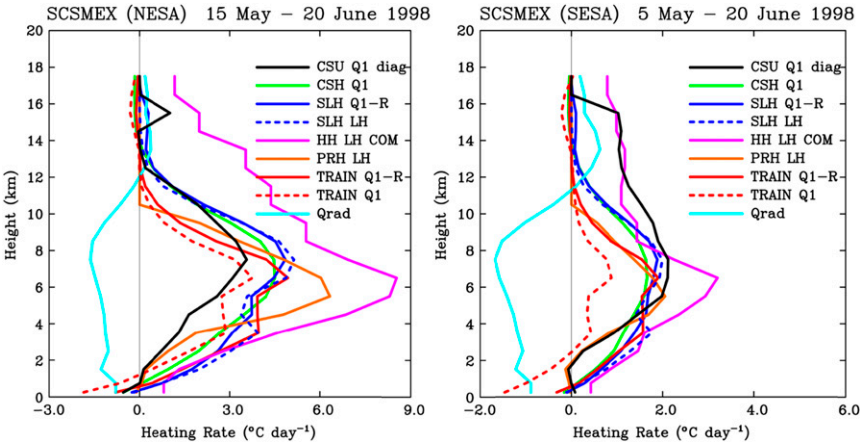

FIG. 2-5. Space–time-averaged heating profiles for the (left) case 1a (SCSMEX-NESA) and (right) case 1b (SCSMEX-SESA) regions. Profiles for different heating terms are obtained from five different satellite algorithms: CSH (solid green), HH (solid violet), TRAIN (solid red) and TRAIN + L'Ecuyer's Q_R (dashed red), SLH (solid and dashed blue), and PRH (solid orange). Q_1 profiles from CSU's diagnostic calculations are the solid black lines (DIAG) from within the NESA/SESA sounding networks. Satellite-derived Q_R profiles from CSU (Qrad, solid turquoise line,) are a gridded product.

conducted in May and June 1998. One of the main underlying scientific objectives of the experiment was to help validate TRMM precipitation and LH algorithms (i.e., vertical profiles of multihydrometeor densities, rain rates, and LH). Diagnostic Q_1 calculations based on the sounding networks were provided by Professor Richard Johnson at Colorado State University (Johnson and Ciesielski 2002; Ciesielski and Johnson 2006).

Two examples of validation results are presented in Fig. 2-5 for the SCSMEX NESA and SESA regions. These diagrams illustrate space–time-averaged vertical profiles of different heating terms obtained from the five different algorithms (i.e., Q_1 from CSH, LH from HH, Q_1 and $Q_1 - Q_R$ from TRAIN, $Q_1 - Q_R$ and LH from SLH, and LH from PRH). In addition, the sounding-diagnosed (DIAG) mean Q_1 profile produced by Colorado State University (CSU) is shown for comparison. For NESA, the results indicate that 1) only SLH exhibits close agreement with the diagnostic (i.e., DIAG) altitude of peak heating; 2) CSH, SLH, and TRAIN show close agreement with each other between low and middle levels; 3) CSH, HH, TRAIN, and PRH exhibit close agreement in the altitude of peak heating among themselves; and 4) all satellite algorithms except HH exhibit relatively close agreement in amplitude of peak heating among themselves, whereas HH exhibits considerably larger amplitude. In the case of SESA, the results indicate that 1) HH and TRAIN exhibit very close agreement with each other in terms of level of peak heating; 2) CSH exhibits close and SLH very close agreement with the DIAG amplitude of peak heating, although the DIAG peak heating layer is somewhat broader aloft than either those of CSH or SLH (or any algorithm); 3) HH is the only algorithm to exhibit positive upper-level heating similar to DIAG, but it also exhibits the largest amplitude of peak heating relative to the other algorithms; 4) Q_R-augmented TRAIN's Q_1 term exhibits the smallest amplitude of peak heating relative to the other algorithms; 5) PRH's lower-level heating agrees well with DIAG; and 6) all of the other algorithms except TRAIN Q_1 have small low-level heating. It should be noted that in addition to the algorithms themselves, differences between the retrieved and observed profiles could also arise from insufficient satellite sampling of the budget domain both in space and time. The inconsistency of the physical quantities of the results (i.e., having different heating products from different heating algorithms) must also be resolved in future intercomparisons.

Table 2-4 lists the altitude of maximum mean heating for the algorithm retrievals and the diagnostic calculations including other cases from a validation study. For all algorithms except HH, the stratiform percentage is needed as a crucial term in determining the respective altitude of peak heating. Generally, a greater stratiform percentage is associated with a higher altitude of maximum heating. For the HH algorithm, which derives its LH profile from the vertical derivative of total rain mass flux adjusted by any cloud layer lift or descent, its level of peak heating is largely determined by the height at which the rain mass flux begins to decrease upward. For several cases, the altitudes of maximum mean heating

TABLE 2-4. Altitude of maximum mean heating (km). Diagnostic Q_1 is calculated from both within the associated sounding arrays and the gridded rectangular study areas for the two SCSMEX cases but only for the associated sounding arrays for KWAJEX and ARM. The SCSMEX cases have two values: one value is for the entire period over the entire grid and the other only when there is good sounding coverage.

Case	CSH (Q_1)	HH (LH)	TRAIN (Q_1, $Q_1 - Q_R$)	SLH ($Q_1 - Q_R$, LH)	PRH (LH)	Diagnostic (Q_1)
SCSMEX–NESA	6.6	6.6	6.5, 6.6	7.5, 7.5	6.5	7.6, 7.7
SCSMEX–SESA	7.5	6.6	6.7, 6.6	7.6, 7.6	6.0	6.5, 6.7
KWAJEX	6.7	5.5	—, 3.6/6.5 (2 max)	7.5, 7.5	6.6	4.5
ARM–spring 2000	7.0	3.0	—	5.5, 5.6	4.5	6.0
ARM–summer 2002	6.5	5.5	—	5.6, 5.6	5.6	8.1

for the algorithms are within 1 km of the diagnostic peak heating levels. However, greater departures are also found, particularly for the less robust KWAJEX case[7] in which the diagnostic calculation indicates a 4.5-km level of maximum heating. Future work will be required to determine if this seemingly low altitude for maximum heating is actually realistic or a bias in the KWAJEX diagnostic analysis. In addition to mean profiles, CFADs (contoured frequency with altitude diagrams; Yuter and Houze 1995) are another useful way to validate LH profiles by comparing heating PDFs.

5. Applications of LH products

A special collection on TRMM diabatic heating was published in the *Journal of Climate*; it comprises papers that derive, test, and compare different diabatic heating products derived from TRMM data. These papers highlight the challenges in separating contributions from deep convective, stratiform, and shallow convective clouds in using TRMM-derived products to study the distribution of diabatic heating and its impact on atmospheric circulations in the tropics. Table 2-5 lists the authors and titles of the papers published in this special collection. In this section, some of the applications of TRMM heating data are highlighted from these papers.

a. Comparing TRMM algorithm, sounding and reanalysis estimates of latent heating profiles over the tropics

Our knowledge of vertical structures of tropical diabatic heating is limited. Vertical structures of diabatic heating from numerical models, including data assimilation products, are strongly influenced by cumulus parameterization, a significant source of model error and uncertainty. Observational (indirect) estimates of diabatic heating profiles as Q_1 using radiosonde data (Yanai et al. 1973) or radar data (Mapes and Houze 1995; Mather et al. 2007; Schumacher et al. 2007) from field campaigns are rare and do not provide a global perspective on the long-term means and variability of vertical diabatic heating structures. On the other hand, heating profiles from TRMM retrievals or data assimilation products provide global and long-term coverage. Their reliability must be quantitatively assessed for their proper application. Their similarities and disagreement define an uncertainty envelope of our current knowledge of diabatic heating. Hagos et al. (2010) systematically compared diabatic heating profiles derived from TRMM, sounding observations, and global reanalyses, and their results are summarized here.

1) DATA

Time series of Q_1 estimated from radiosonde observations are available from eight field campaign networks (Table 2-2). All data represent averages over areas of roughly 10^3–10^5 km^2 in different tropical climate regimes (Fig. 2-3), including open ocean with small or no islands (GATE, TOGA-COARE, KWAJEX, and MISMO), coastal and monsoon regions (SCSMEX, TWP-ICE), and continental rain forest (LBA). The time interval of all Q_1 data is 6 h and the vertical levels are from 1000 to 100 hPa with a 25-hPa increment.

Estimates of diabatic heating associated with precipitation and total diabatic heating were made from several global reanalyses, including three recently released high-quality reanalysis datasets [ERA-Interim (hereinafter ERA-I), MERRA, and CFSR] as well as earlier reanalysis datasets (NCEP-2, JRA-25, and ERA-40). All reanalysis products overlap with TRMM from 1 January 1998 to 31 December 2007. For all reanalyses, diabatic heating was estimated as Q_1 from the 3D wind and temperature fields. CFSR and MERRA provide direct output of total diabatic heating (Q_T[8]).

[7] KWAJEX had a relatively low ratio of satellite sampling relative to the sounding array.

[8] Q_T is total diabatic heating direct output from reanalyses as a component of temperature tendency. Q_1 is calculated as the residual of the heat budget.

TABLE 2-5. Authors and titles of papers published in the special collection on TRMM diabatic heating in the *Journal of Climate*. Dr. Tony Del Genio was a guest editor for this special collection.

Authors	Topic/title
T. L'Ecuyer and G. McGarragh	A 10-year climatology of tropical radiative heating and its vertical structure from TRMM observations
S. Shige, Y. N. Takayabu, S. Kida, W.-K. Tao, X. Zeng, C. Yokoyama, and T. L'Ecuyer	Spectral retrieval of latent heating profiles from TRMM PR data. Part IV: Comparisons of lookup tables from two- and three-dimensional cloud-resolving model simulations
M. Grecu, W. Olson, C.-L. Shie, T. L'Ecuyer, and W.-K. Tao	Combining satellite microwave radiometer and radar observations to estimate atmospheric heating profiles
W.-K. Tao, S. Lang, X. Zeng, S. Shige, and Y. N. Takayabu	Relating convective and stratiform rain to latent heating
T. Krishnamurti, A. Chakraborty, and A. K. Mishra	Improving multimodel forecasts of the vertical distribution of heating using the TRMM profiles
X. Jiang, D. Waliser, W. Olson, W.-K. Tao, T. L'Ecuyer, J.-L. Li, B. Tian, Y. L. Yung, A. Tompkins, S. Lang, and M. Grecu	Vertical heating structures associated with the MJO as characterized by TRMM estimates, ECMWF reanalyses, and forecasts: A case study during 1998/99 winter
S. Hagos, C. Zhang, W.-K. Tao, S. Lang, B. Olson, Y. Takayabu, S. Shige, M. Katsumata and T. L'Ecuyer	Estimates of tropical diabatic heating profiles: Commonalities and uncertainties
K.-M. Lau and H.-T. Wu	Characteristics of precipitation, cloud, and latent heating associated with the Madden–Julian oscillation
M. Zuluaga, C. Hoyos, and P. Webster	Spatial and temporal distribution of latent heating in the South Asian monsoon region
Y. N. Takayabu, S. Shige, W.-K. Tao and N. Hirota	Shallow and deep latent heating modes over tropical oceans observed with TRMM PR spectral latent heating data
Y.-M. Kodama, M. Katsumata, S. Mori, S. Sato, Y. Hirose, and H. Ueda	Climatology of warm rain and associated latent heating derived from TRMM-PR observations
S. Xie, T. Hume, C. Jakob, S. A. Klein, R. B. McCoy and M. Zhang	Observed large-scale structures and diabatic heating and drying profiles during TWP-ICE
R. H. Johnson, P. E. Ciesielski, T. S. L'Ecuyer, and A. J. Newman	Diurnal cycle of convection during the 2004 North American Monsoon Experiment

The TRMM heating products are available only in regions with precipitation (and hence are predominantly LH). When compared to the TRMM heating retrievals, diabatic heating from the reanalyses is set to zero if there is no precipitation. The focus of the study is the vertical structure of diabatic/LH in the tropics, not its actual magnitude and spatial distribution. For comparison, the TRMM products are regridded onto the (2.5° × 2.5°) horizontal reanalysis grids and interpolated onto 17 reanalysis pressure levels. In comparing heating profiles from the soundings with those from the TRMM and reanalysis products, one should bear in mind that the estimates from the TRMM and reanalysis products are either purely LH (PRH) or diabatic heating only when there is precipitation (SLH, CSH, TRAIN, NCEP-2, JRA-25, ERA-40, and MERRA), while those from the soundings are purely total heating. For brevity, however, all the variables (Q_T, Q_1,[9] and LH) are referred to as diabatic heating.

2) GENERAL CHARACTERISTICS

Several tropical precipitation regions (Fig. 2-6) were defined to facilitate discussions on regional heating characteristics. Global time means of tropical diabatic heating profiles can be perceived as averages over these regions (with LH dominating, suitable for TRMM retrievals) or the entire tropics (with both latent and radiative heating from the reanalyses). Mean profiles averaged over the precipitation regions reveal that the largest disagreement among the TRMM retrievals and reanalyses is low-level heating. Some products (e.g., SLH, TRAIN, NCEP-2, MERRA, and JRA-25) exhibit distinct or even dominant heating peaks below the 700-hPa level, which are very weak or absent in others (Fig. 2-7). Another related disagreement is the number of heating peaks in the vertical. Some products show two or more peaks (e.g., SLH, TRAIN, MERRA, and JRA-25) and others only one. These two major disagreements among the TRMM retrievals and reanalyses can be repeatedly seen in various comparisons with different configurations. Global zonal mean heating profiles from the reanalyses agree with each other well in their contrast between the tropics and extratropics and between the oceans and land (Fig. 2-8). However, large disagreement in their heating peaks, either the level or the number, is obvious.

Another way to characterize the heating profiles is to compare them as functions of the precipitation rate. In the Atlantic region, for example, TRMM and reanalysis

[9] Q_R is relatively small in regions of large precipitation.

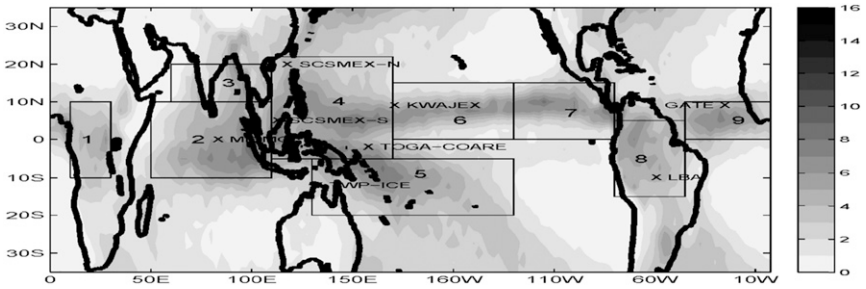

FIG. 2-6. 10-yr mean precipitation from TRMM (3G68, mm day^{-1}). Boxes indicate the analysis domains. Locations of the field campaign sounding sites are marked by an X. Adapted from Hagos et al. (2010).

estimates, except PRH, show their heating peaks becoming elevated as the precipitation rate increases (Fig. 2-9). This relationship between the LH profiles and the precipitation intensity is in agreement with the results of Short and Nakamura (2000), which showed a correlation of 0.71 between PR echo-top height and conditional rain rate over the Atlantic and eastern Pacific Oceans. The increase in heating peak with rain rate is gradual in some products (e.g., SLH, TRAIN, and MERRA) but fast or even abrupt in others (e.g., CSH, ERA-40, JRA-25). Double peaks exist at certain rain rates in PRH, ERA-40, and JRA-25. The only estimates that produce significant stratiform cooling in the lower troposphere at high precipitation rates are PRH and TRAIN. A similar diagnostic was performed over Africa (Hagos et al. 2010; not shown). There is no low-level heating peak in any of the three TRMM estimates (TRAIN has no estimate of heating over land). In the lower tail of precipitation rates, the TRMM estimates have elevated heating and low-level cooling. In the reanalysis estimates, there is an abrupt transition in the diabatic heating profiles with sensible heat fluxes and radiative cooling dominating below about 1 mm day^{-1} and elevated LH at higher precipitation rates, because shallow LH is essentially absent there. Therefore in general, these estimates differ from each other mainly in where their heating peaks are and whether they have just a single peak or double peaks. The differences in the oceanic low-level heating among the TRMM products are, however, in the amount and structure of the shallow LH, which is most abundant in SLH, small in CSH and TRAIN, and essentially absent in PRH. On the other hand, while all the reanalyses have low-level heating peak near the surface, the magnitude and height vary.

3) TEMPORAL VARIABILITY

The temporal characteristics of daily heating profiles can be described in terms of their primary modes of variability. Such primary modes can be extracted using various forms of empirical orthogonal function (EOF) analysis (Zhang and Hagos 2009; Hagos et al. 2010). Two leading rotated EOF modes—one deep, one shallow—emerge from heating profiles based on sounding observations, TRMM retrievals, and reanalyses (Fig. 2-10). The differences among the mean profiles (Figs. 2-10a,e) are larger than those among the deep modes (Figs. 2-10b,f) as well as the shallow modes (Figs. 2-10c,g). However, there are discrepancies among them. The deep modes of CSH and PRH are outliers in their lack of heating at low levels. The peak of the deep heating of PRH, CSH, and NCEP-1 (at 300 hPa) is higher than that of the sounding average (near 400 hPa). For the shallow modes, PRH has a peak near 600 hPa and JRA-25 at 850 hPa while those of the other estimates as well as the soundings are at 700 hPa.

For the purpose of interpreting the variability characteristics of LH, a diabatic heating profile is designated as due either to radiation, if the vertically integrated diabatic heating is negative, or to latent heat release. In a tropical convective region such as the western Pacific warm pool, the vertical structure of heating is primarily determined by LH. An EOF analysis shows that almost all of the variability in total diabatic heating is due to LH. For both, the first two EOF modes explain about 95% of the variance (Hagos et al. 2010). This is not surprising because, while the vertical structure of LH varies significantly, the profile of clear-sky cooling shows little variability.

An oblique rotated EOF (OREOF) analysis yielded the first mode resembling a stratiform heating profile with low-level cooling and the second OREOF resembles convective heating (Fig. 1 in Schumacher et al. 2007). Almost the entire diabatic heating data are composed of the two profiles. This is not by accident. If indeed mesoscale LH is primarily composed of stratiform and convective heating, they naturally should constitute the large-scale diabatic heating as well. Hagos et al. (2010) demonstrated that the bimodal variability and the structure of the leading EOF modes alone can

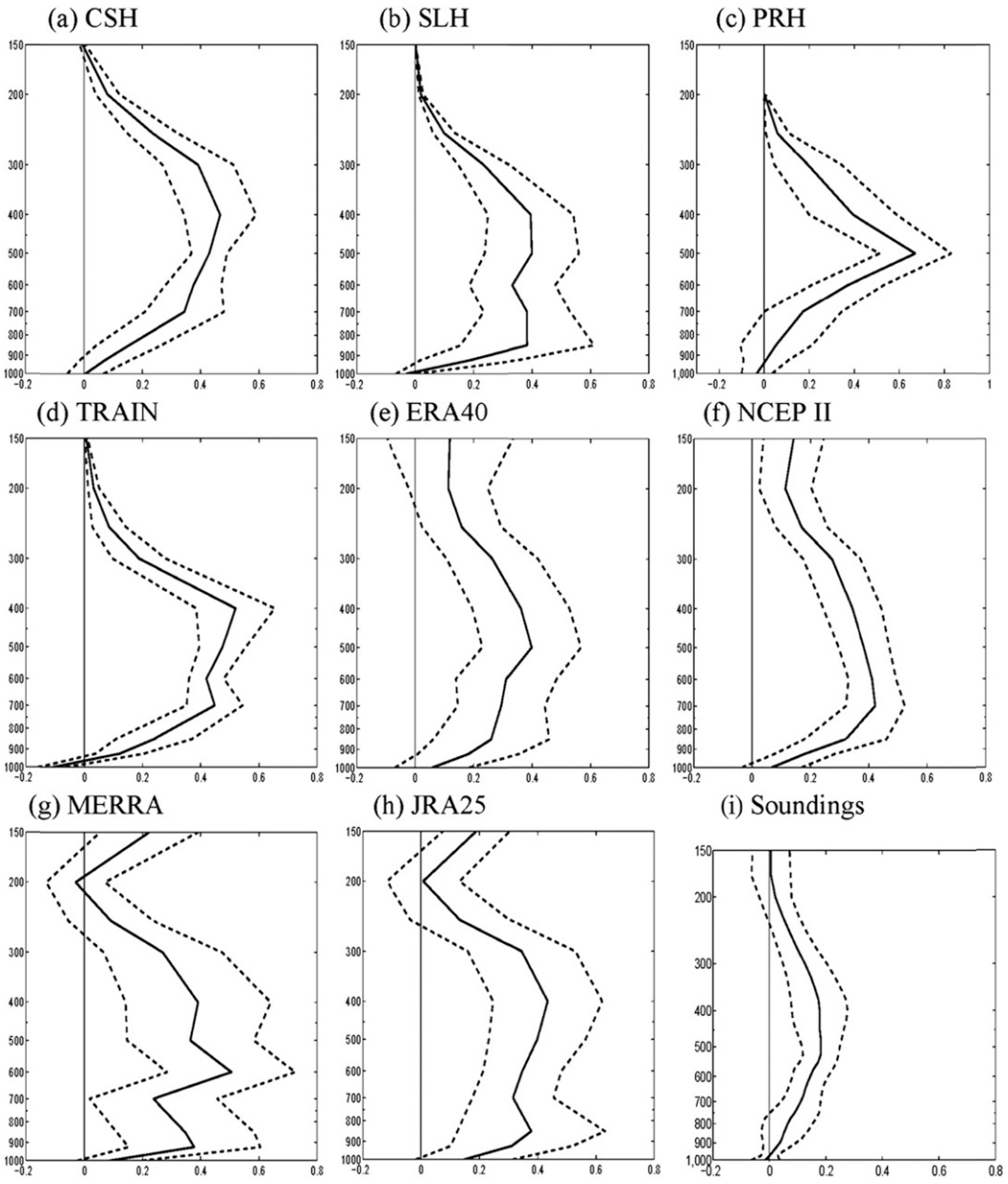

FIG. 2-7. (a)–(h) Normalized mean heating profiles averaged over the tropical precipitation regions (shown by the boxes in Fig. 2-10) and (i) the mean profile of the diabatic heating from all the soundings. The normalization was done by dividing each heating profile by its norm, which is the square root of the sum of the squared heating at all levels. Dashed lines are the standard deviation. Adapted from Hagos et al. (2010).

represent the mean diabatic heating in different climate regimes of the tropics (Fig. 2-11). For all the sounding-based heating time series, the two modes account for almost all their means. It follows that the total heating is primarily composed of these two building blocks.

Comparisons of diabatic/LH derived from in situ soundings, satellite observations, and global reanalyses have revealed that, in general, they agree with each other on their bimodal variability. The common bimodal behavior comes from the composition of large-scale heating by convective and stratiform clouds. This is implicitly built into TRMM LH algorithms that depend on PR reflectivity; hence, the bimodal variability in those products is not surprising. The commonalities among the various products, however, appear to end at the bimodal variability. The structures of the two leading modes, the mean profiles, and the seasonal cycle vary significantly among the products. The large

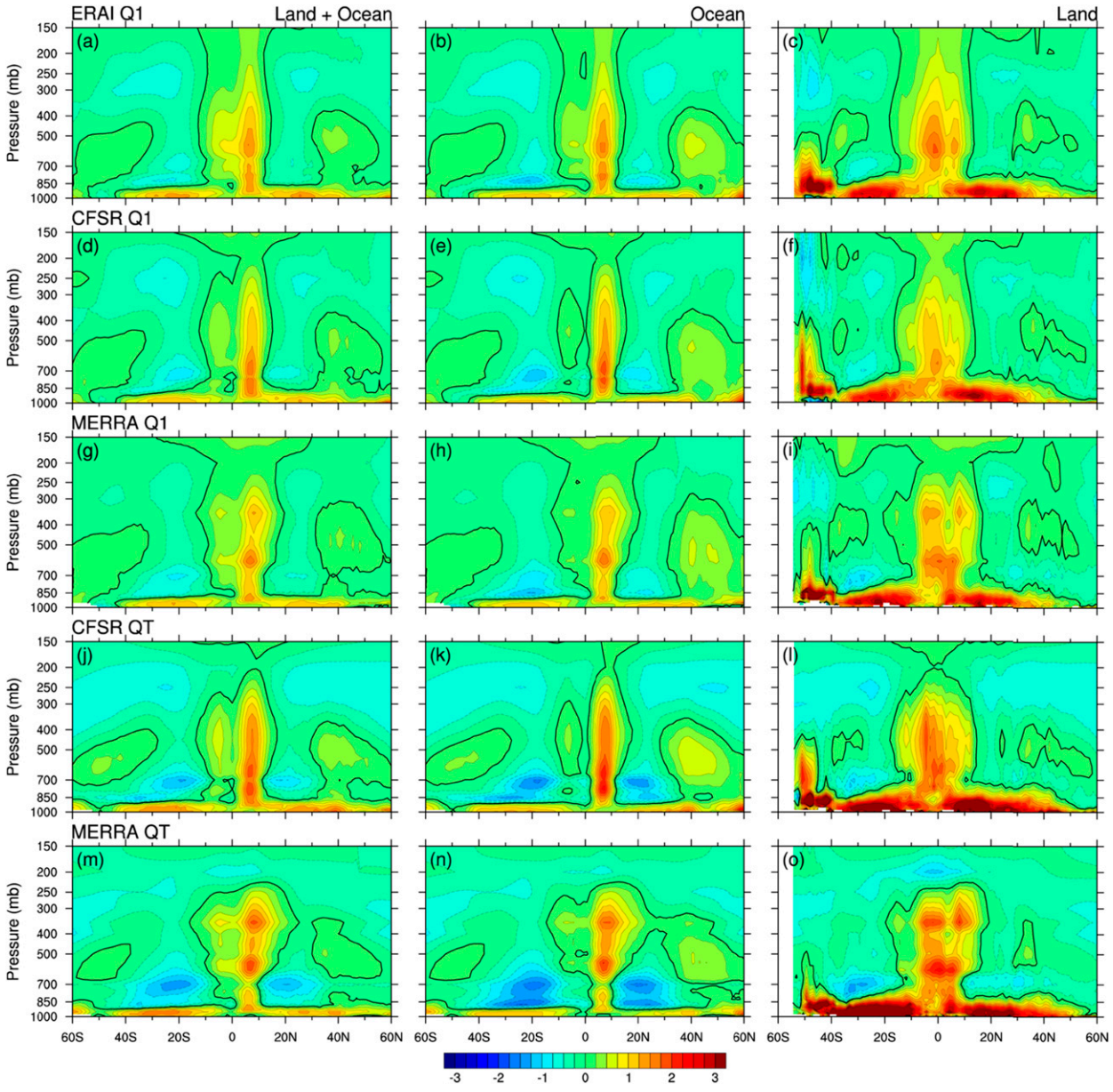

FIG. 2-8. (left) Time and zonal means of land and ocean diabatic heating (K day^{-1}) from (top to bottom) ERAI Q_1, CFSR Q_1, MERRA Q_1, CFSR Q_T, and MERRA Q_T; (center), (right), as at left, but respectively over the oceans only and land only. Adapted from Ling and Zhang (2013).

uncertainties defined by their disagreement inevitably affect their applications. The limited availability of sounding-based heating profiles and the large spatial variability in the vertical structure of diabatic and LH preclude any assumption on the realism of diabatic and LH profiles from TRMM and reanalyses in a region without any observations. Evaluation of diabatic and LH profiles from TRMM and reanalyses must be done in the context of their related large-scale circulation.

b. MJO life cycle

1) VERTICAL DIABATIC HEATING STRUCTURE OF THE MJO THROUGH ITS LIFE CYCLE

Using diabatic heating datasets from three TRMM-based estimates (TRAIN, SLH, CSH) and three recent reanalyses (ERA-I, MERRA, CFS-R), Jiang et al. (2011) conducted a composite analysis of vertical anomalous heating structures associated with the MJO based on

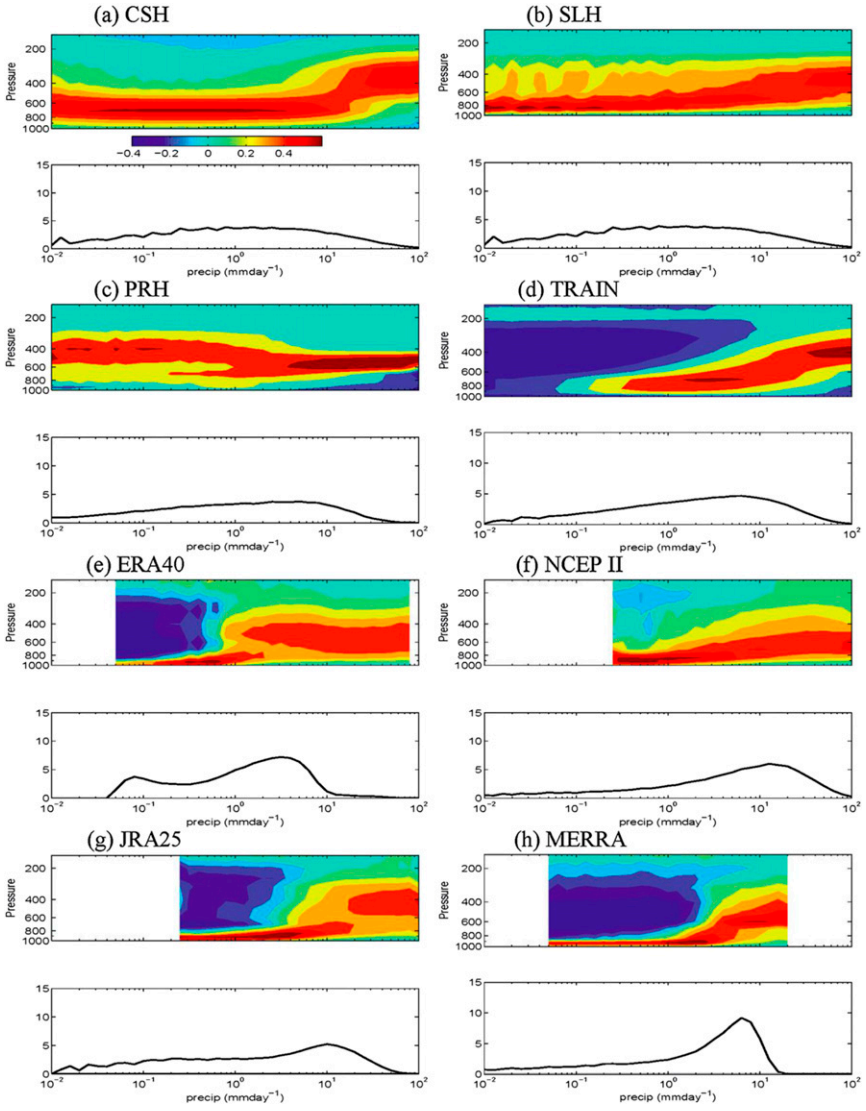

FIG. 2-9. Normalized LH profiles as functions of precipitation intensity (units of standard deviation) and the PDF of precipitation over the Atlantic. The dashed lines indicate a precipitation rate of 1 mm day^{-1}. For the soundings, vertically integrated diabatic heating is used as a proxy for precipitation. Adapted from Hagos et al. (2010).

strong MJO events during boreal winter (November–April) from 1998 to 2007/08. The strong MJO events were selected and their phases (ranging from 1 to 8) determined by the real-time multivariate Wheeler-Hendon index (Wheeler and Hendon 2004; hereinafter the WH index). Figure 2-12 illustrates vertical-temporal anomalous MJO heating profiles (shaded) based on six datasets over the western Pacific (WP; 150°–160°E) and eastern equatorial Indian Ocean (EEIO; 80°–90°E), all averaged over 10°S–10°N. The black curve in each panel denotes the evolution of TRMM 3B42 rainfall anomalies (scales on the right). The results suggest that, over the WP, the heating profiles based on three reanalyses exhibit a similar vertical tilting structure (Figs. 2-12a–c). The low-level heating below 800 hPa appears around phase 3 and peaks at phase 4 prior to the maximum MJO convection in phase 5. Meanwhile, a maximum heating near 450 hPa after phase 5 is discerned in all three reanalysis datasets. In addition to the upper-level heating maximum, a second peak around 600 hPa is also apparent in MERRA (Fig. 2-12b). In contrast, the vertical tilt in the heating profiles varies among the three TRMM products. While the tilt is evident in CSH, the heating does not extend to the upper troposphere as in other datasets (Fig. 2-12f). Although the emergence of shallow heating prior to maximum convection is also discerned in the SLH

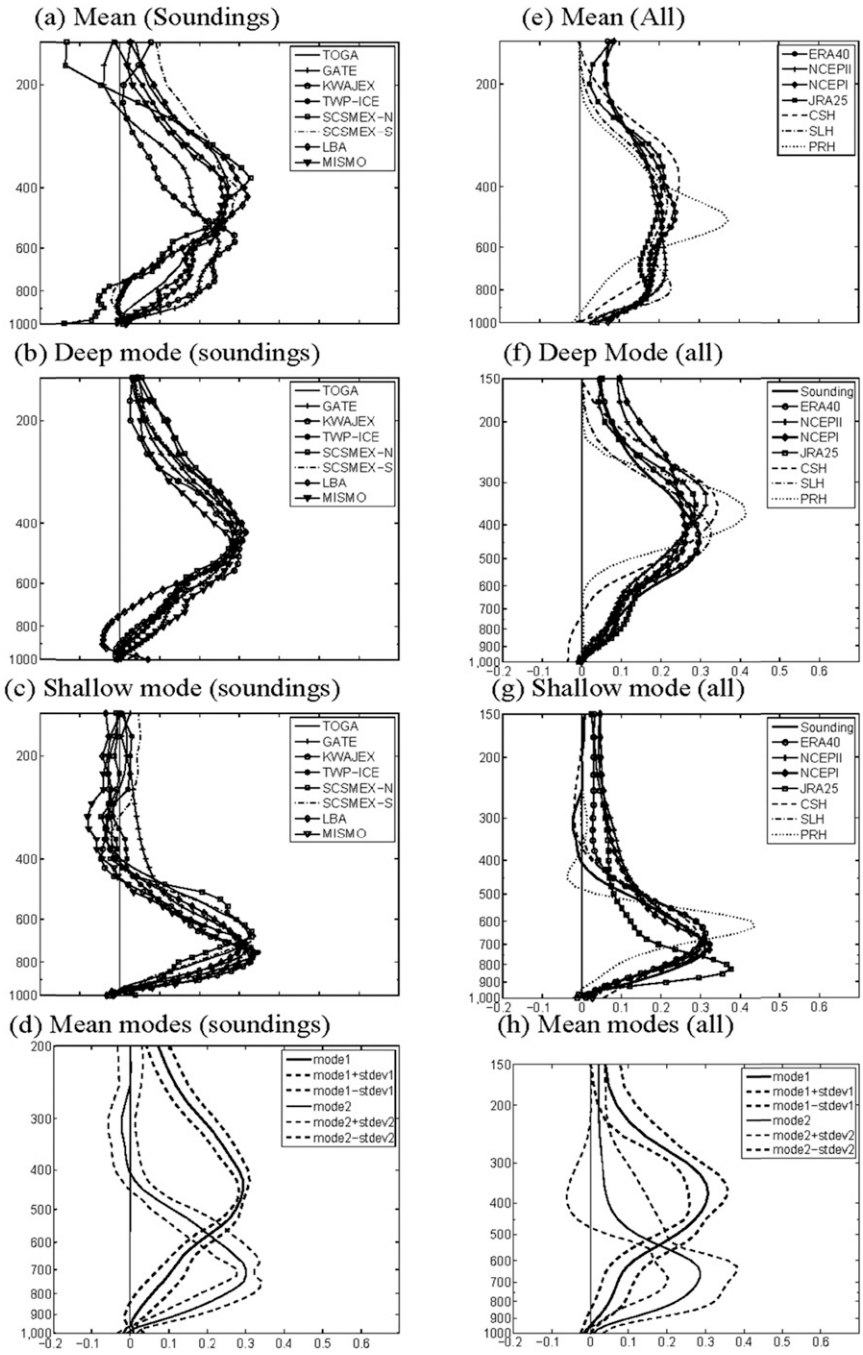

FIG. 2-10. (a) Mean, (b) deep, (c) shallow, and (d) the average of the deep and shallow mode profiles and their standard deviations from the soundings. (e)–(h) As in (a)–(d), but for the reanalyses and TRMM products. Adapted from Hagos et al. (2010).

heating ($Q_1 - Q_R$) profiles, it has much weaker amplitude below 600 hPa (Fig. 2-12e). Meanwhile, a rather weak tilt is seen in the TRAIN profiles (Fig. 2-12d); instead of a slight lag in maximum convection evident in other datasets, the upper-level heating maximum is largely in phase with convection in TRAIN.

Over the EEIO, the transition from a shallow to deep heating structure during MJO evolution is again evident based on the three reanalysis datasets (Figs. 2-12g–2-16i). However, some differences in the upper-level heating profiles are noticed between the EEIO and WP. While the heating maxima around 400 hPa lag the

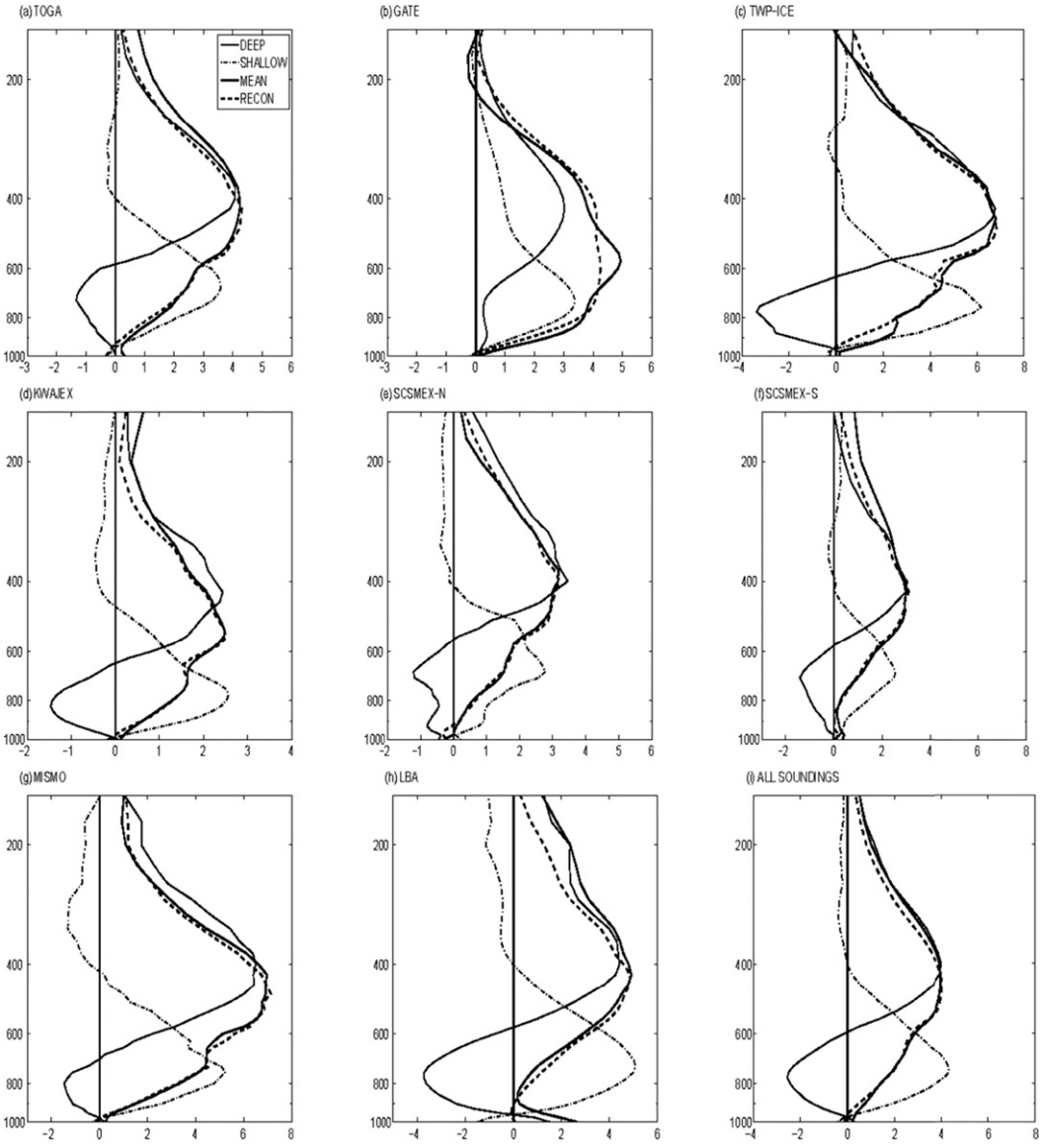

FIG. 2-11. Reconstruction of mean sounding profiles using the first two oblique rotated EOFs. Adapted from Hagos et al. (2010).

rainfall peaks over the WP, they appear with the peaks in MJO convection over the EEIO (cf. Figs. 2-12a–c and 2-12g–i). The vertical transition from shallow to deep heating structures as seen in the reanalyses is not readily apparent in three of the TRMM-based datasets over this region (Figs. 2-12j–l).

Differences in vertical heating structures of the MJO between TRMM estimates and reanalyses are also noted in a similar composite study by Ling and Zhang (2011). By illustrating vertical/temporal MJO heating structures at three longitudes (90°, 120°, and 150°E), but averaged over 15°S–15°N instead of 10°S–10°N as in Fig. 2-12, significant differences in composite vertical MJO heating structures were found among several reanalysis datasets in addition to differences between reanalyses and TRMM estimates as mentioned above.

2) RAIN AND CLOUD CHARACTERISTICS AND LH PROFILES DURING DIFFERENT PHASES OF THE MJO

Lau and Wu (2010) used TRMM observations to examine the characteristics of clouds, rainfall and LH associated with the eight MJO phases defined by the real-time multivariate WH index. In a 2D cloud–rain probability distribution function (PDF) using brightness temperature (Tb) and echo-top height (ETH) for the

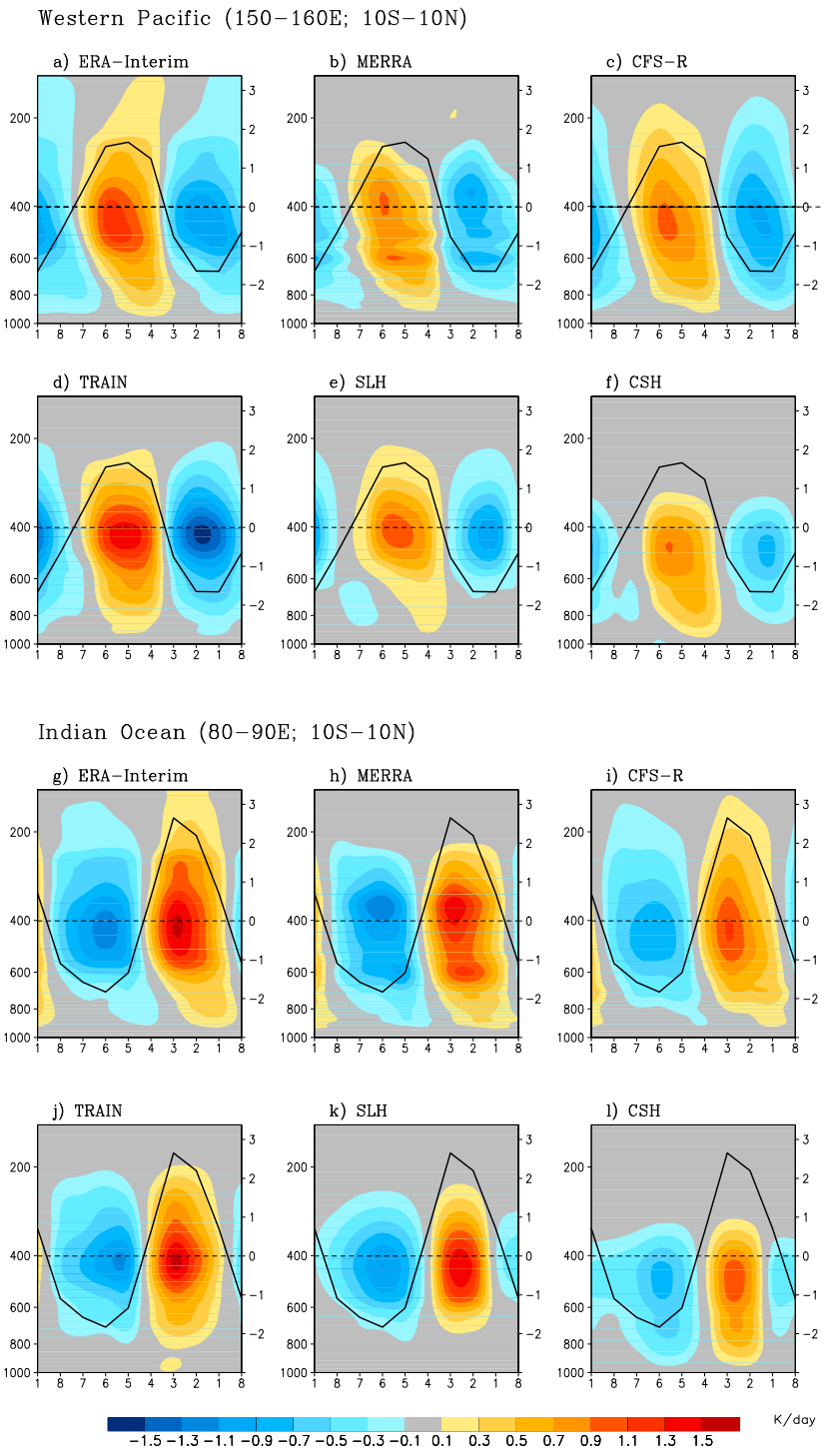

FIG. 2-12. Vertical–temporal (MJO phase) evolution of anomalous heating Q_1 or $Q_1 - Q_R$ for TRMM SLH (shaded, in K day^{-1}) over the (a)–(f) WP (150°–160°E) and (g)–(l) EEIO (80°–90°E) based on three reanalysis datasets and three TRMM estimates. The black curve in each panel represents the evolution of TRMM 3B42 rainfall anomalies (mm day^{-1}; see scales on right y axis). All variables are averaged over 10°S–10°N. The time (MJO phases) in the x axis of each panel runs from right to left so that these plots also mimic longitude–height cross sections for an eastward moving system. Adapted from Jiang et al. (2011).

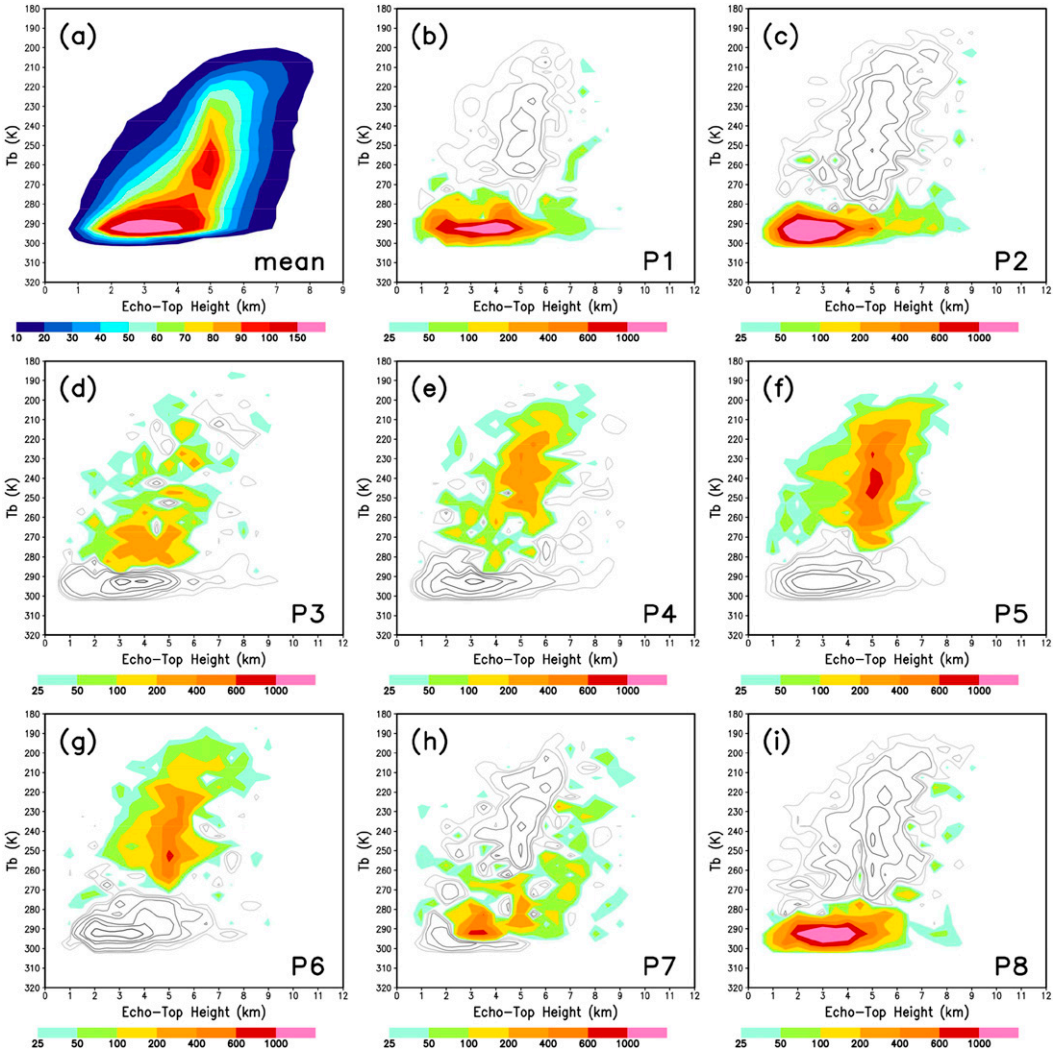

FIG. 2-13. Joint PDF (JPDF) of Tb and ETH over the equatorial western Pacific: (a) mean state of the eight MJO phases and (b)–(i) the difference between the JPDF for each of the eight phases (P1–P8) and the mean state. Positive values are color shaded and negative values are contoured. The units for the mean state are in 0.01% of the total occurrence counts. For P1–P8, the units are number of counts. Adapted from Lau and Wu (2010).

region 10°S–10°N, 120°–150°E (Fig. 2-13), a bimodal distribution with an abundance of warm-low and cold-middle cloud and rain types is evident for all active (amplitude of the WH index >1) phases of the MJO (Fig. 2-13a). The highest population is from the warm-low type, with Tb > 273 K and ETHs below the freezing level (~5 km). The cold-middle type, identified as congestus, has a high population centered rather narrowly near the melting level with a wide range of cloud tops colder than 273 K. Four main regimes—WL (warm-rain low-level cloud), MM (mixed-phase rain, middle-level cloud), CM (cold cloud-top and medium storm height), and CH (cold rain, high-cloud)—defined based on Tb and ETH, are consistent with the four tropical precipitation systems—shallow, cumulus congestus, deep stratiform, and deep convective—classified in the observed study of Masunaga et al. (2005). There is also a nonnegligible warm rain, middle-level cloud (WM) regime, which counts for about 9% of the total population.

The changes in rain characteristics over the MJO life cycle, shown in anomalous PDFs defined as the deviation of the PDF at a particular phase from that of the mean in (Figs. 2-13b–i), are characterized by the following stages. (a) An abundant occurrence of the WL type (color shaded) and a large deficit in the MM and CM types (black and white contours) during the early build-up stage (i.e., phases 1 and 2) is followed by a transition from a bottom-heavy to a top-heavy distribution with a large increase in MM and CM types representing an increase in mixed-phase precipitation due

TABLE 2-6. The characteristics of MJO phases in terms of brightness temperature (Tb), echo-top height (ETH), and type of cloud systems. WL stands for warm-rain low-level cloud, MM for mixed-phase rain, middle-level cloud, CM for cold cloud-top and medium storm height, and CH for cold rain, high-cloud.

Phase(s)	Life cycle	Tb (K)	ETH (km)	Types of cloud system
1–2	Genesis	290–300	2.5–4.5	Abundant occurrence of WL
3–4	Developing	260–280	4.5	Large increase of MM and CM
5	Mature or peak convection	<275	>5	Large increase of CM and CH
6	Start of decaying	Wide range of Tb	>5	
7	Decaying	<275	>6–7	Increase of WL
8	Similar to phase 1	290–300	2.5–4.5	WL

to developing deep convection (phases 3 and 4). (b) At the maximum large-scale organization (phase 5), the CM and CH types increase considerably, with the coexistence of mixed-phase and ice-phase precipitation and shallow, middle, and deep convective clouds. (c) Deep convection starts to diminish in phase 6, with the convective system dominated by CM and MM types and the presence of both precipitating and nonprecipitating high-level anvil clouds, and continues in phase 7 with a substantial amount of deep convective rain (ETHs above 6–7 km) and appearance of low-level rain. (d) The completion of an MJO cycle occurs with the WL-type rain reestablishing itself in phase 8 and continuing into phase 1 again. Table 2-6 shows the main characteristics of each MJO phase in terms of Tb, ETH, and cloud system type.

Figure 2-14 shows mean TRMM daily LH profiles[10] as well as the anomalous heating (deviation in each phase from the mean) during the eight phases of the MJO cycle. Contributions from heating with ETHs less than and greater than 5 km are shown separately to demonstrate the relative contributions from shallow (liquid-phase and mixed-phase rain) and deep (ice-phase and mixed-phase rain) convection. The magnitude of the mean heating by shallow convection is about 30%–35% of that due to deep convection. In phases 1 and 2, anomalous lower tropospheric heating is due equally to shallow convection (ETH < 5 km) and low-level heating of deep convection (ETH > 5 km). A switch from a bottom-heavy (warm and shallow convective rain) to a top-heavy (mixed convective and stratiform rain) heating profile occurs from phases 2 through 4, consistent with the cloud PDF distributions shown in Fig. 2-13. The anomalous low-level heating from shallow convection in phase 3 is most likely from the abundant mixed-phase rain. During phases 4 and 5, the heating profiles show maximum heating at about 7–8 km and cooling below 2–3 km, typical of that associated with stratiform rain systems (Houze 1989; Tao et al. 2006; Jakob and Schumacher 2008). In the decaying phases (6 and 7), mid- and upper-tropospheric heating diminishes and low-level heating reverses sign, reflecting the reduction in warm-rain processes with the deep heating profiles changing sign. Phase 8 completes the MJO cycle with a large reduction in deep heating and the beginning of low-level heating processes.

c. *Improving the ability of large-scale models to simulate/predict weather and climate*

The explicit use of TRMM LH information for initialization and/or assimilation in global models is a relatively new research topic. Further study is needed to quantify how much improvement can be obtained in predictions with LH profile-based data assimilation. However, this is worth considering from a theoretical perspective since it is the vertical distribution of diabatic heating that determines the nature of many low-latitude circulations. Thus, it seems reasonable to expect that improved data assimilation techniques involving accurate LH profile data will ultimately improve NWP forecasts on a consistent basis. Two examples are provided to show how TRMM-retrieved LH profiles are being used as data assimilation variables to bring about prediction improvements in global weather and climate models and to improve the understanding of physical processes in tropical circulations.

1) SHALLOW AND DEEP LATENT HEATING MODES AND THE LARGE-SCALE CIRCULATION

Utilizing $Q_1 - Q_R$ data estimated from the SLH algorithm, Takayabu et al. (2010) showed that nondrizzle precipitation over tropical and subtropical oceans consists of two dominant modes of rain systems: deep systems and congestus. They found that while rain from congestus simply increases with sea surface temperature (SST), deep convective precipitation is inhibited by large-scale atmospheric subsidence even though SSTs are warm enough to support congestus. Figure 2-15 compares $Q_1 - Q_R$ at 7.5 and 2 km: the former represents the effect of deep organized precipitation, while the latter represents the effect of congestus rain. Over the central-to-eastern Pacific, in the Southern

[10] Prototype CSH-derived LH was used for this study because the new CSH algorithm was not available at that time.

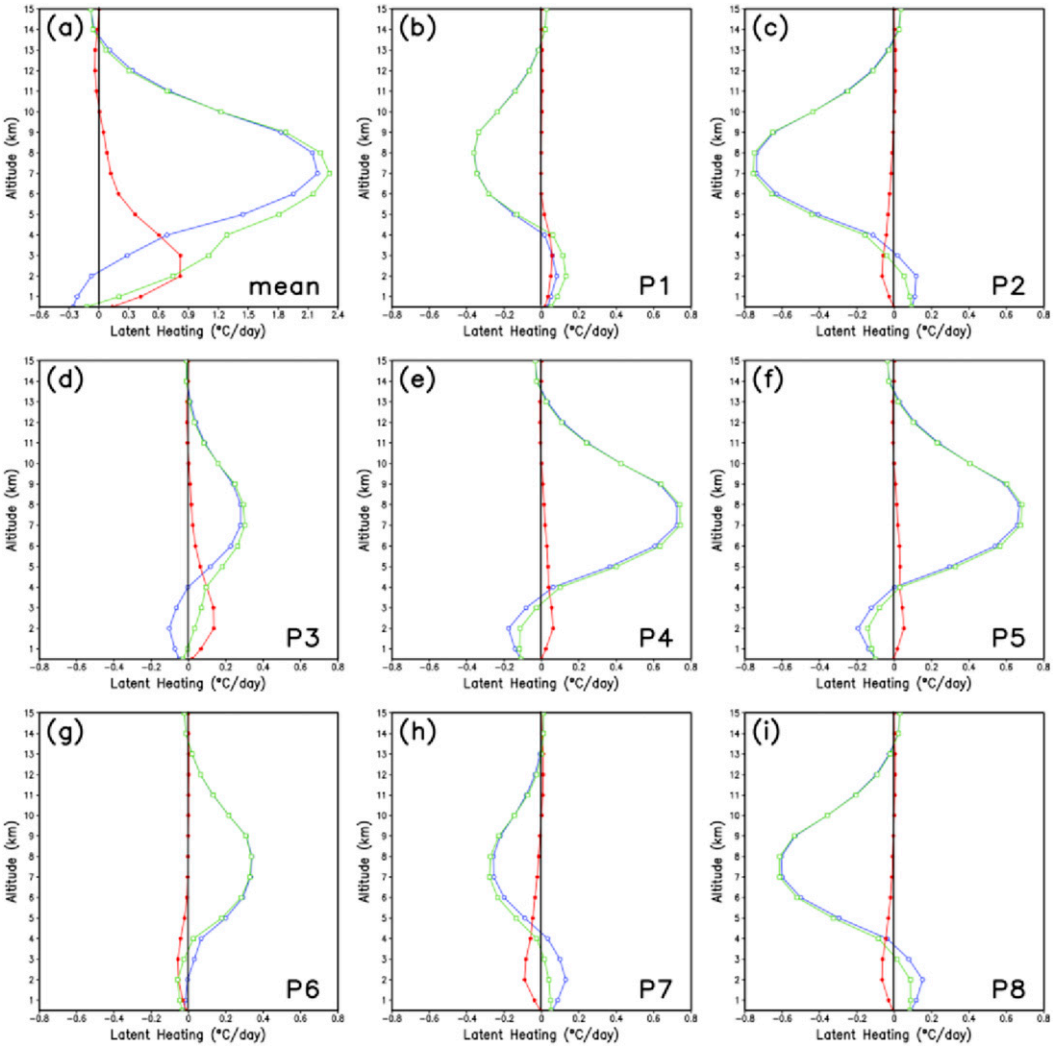

FIG. 2-14. MJO LH profiles based on the CSH algorithm and daily averaged ETH: (a) mean state of the eight MJO phases and (b)–(i) the difference between the heating profile of each phase, P1–P8, and the mean state. The three curves in each panel are red for ETHs < 5 km, blue for ETHs > 5 km, and green for total. Adapted from Lau and Wu (2010).

Hemisphere, along the equator, and also near the Hawaiian Islands, for example, the congestus rain distribution neatly follows the SST distribution, even where deep convective rain is almost completely suppressed.

Figure 2-16 shows 7-yr mean $Q_1 - Q_R$ profiles over 30°N–30°S for September–November stratified against 500-hPa vertical velocity. The results confirm the existence of two dominant modes in tropical nondrizzle precipitation and an effective suppression of the deep mode associated with large-scale subsidence, which is accompanied by middle to lower tropospheric drying. These results are in concert with recent studies indicating significant entrainment of environmental air by cumulus clouds (Sherwood 1999; Zipser 2003; Bretherton et al. 2004; Takemi et al. 2004; Takayabu et al. 2006). A reduction in buoyancy via dry air entrainment prevents cumulus from penetrating above the freezing level by not allowing them to gain additional latent heat from freezing (Zipser 2003). This is possibly why the development to deep convection is discretized at midlevels.

More recently, Hirota et al. (2011) compared the distributions of tropical precipitation from 19 models as part of CMIP3 and found that the double ITCZ bias is linked to the cumulus convection scheme: the more sensitive the deep convective scheme is to midtropospheric humidity, the less double ITCZ bias the model has. This result is consistent with Del Genio et al. (2012), who attributed successful MJO model simulations to adequate representation of deep convection in relation to the midtropospheric humidity. Hirota et al. (2011) showed that the double ITCZ bias is absent in MIROC5, the current version of the climate model developed by the Atmosphere and

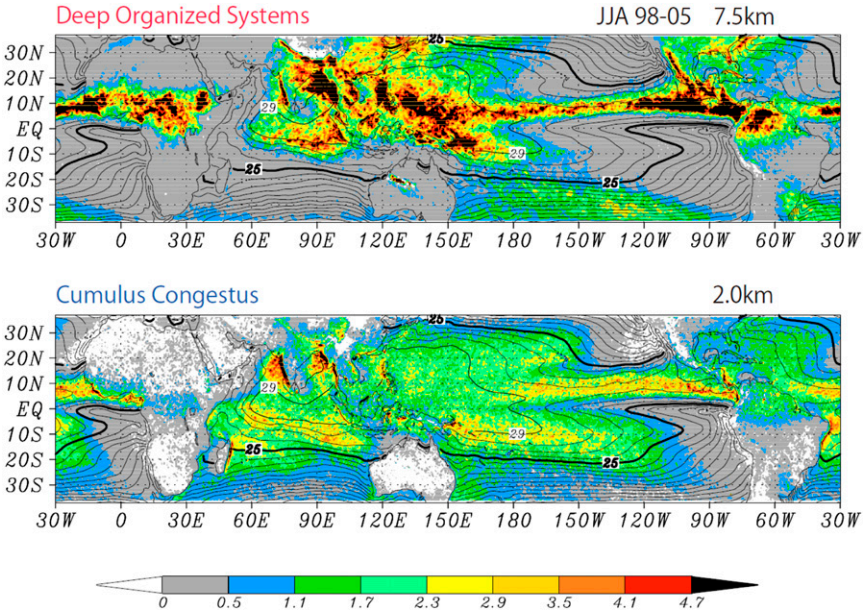

FIG. 2-15. $Q_1 - Q_R$ at (a) 7.5 and (b) 2.0 km averaged for June–August from 1998 to 2007 overlaid on SST (contours). Color scale labels show $Q_1 - Q_R$ values in degrees day^{-1}; SST contour intervals are every 1°C with the 28° and 25°C contours shown in thick lines in the upper and lower panels, respectively. Adapted from Takayabu et al. (2010).

Ocean Research Institute (AORI), National Institute for Environmental Studies (NIES), and the Japan Agency for Marine-Earth Science and Technology (JAMSTEC), with a new entrainment scheme introduced by Chikira and Sugiyama (2010) into the cumulus parameterization. The essential impact of cumulus entrainment on deep precipitation is further examined by Hirota et al. (2014) in a sensitivity study utilizing the atmospheric part of MIROC5. It was confirmed that the entrainment rate controls the double ITCZ even for the same SST distribution.

As shown in Fig. 2-15, congestus heating (Fig. 2-15b) follows the SST, which results in a double ITCZ–like distribution, while the deep heating does not show such a double ITCZ–like distribution (Fig. 2-15a). Deep heating is well suppressed along the equator in the southeastern Pacific, as well as around the Hawaiian Islands, which is consistent with the above interpretation of climate model results. In these two regions, although congestus precipitation is enhanced by relatively warm SSTs, large-scale subsidence with a dry middle troposphere strongly discourages further development of the congestus and suggests that real world cumulus convective systems entrain considerable amounts of environmental air.

2) IMPROVING MONSOON FORECASTS AND MODEL PHYSICS USING THE MULTIMODEL SUPERENSEMBLE APPROACH

The vertical distribution of heating predicted by a suite of global models (Krishnamurti et al. 2007) was improved using a multimodel superensemble technique (Krishnamurti et al. 2000a,b). The same approach but with a suite of mesoscale models in place of global models is being used to construct forecasts of Q_1. A standard version of ARW was used in this study (Krishnamurti et al. 2012). Table 2-7 lists a set of model configurations put together from the available choices of different cumulus parameterizations and microphysics packages within ARW.

The multimodel superensemble has a training and a forecast phase. The training phase covered the period from 1 July to 31 August 2004 and 1 July to 28 August 2005. During the training phase, a superensemble was constructed for the geopotential height z and the temperature T. Note that Q_1 is the substantial derivative of

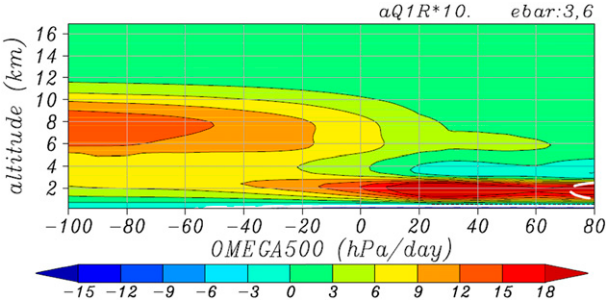

FIG. 2-16. 7-yr conditional mean $Q_1 - Q_R$ profiles stratified with vertical velocity (dp/dt) at 500 hPa averaged for September–November for 30°N–30°S at all longitudes over the ocean in association with all rain. The values for the color scale are scaled by a factor of 10. Adapted from Takayabu et al. (2010).

TABLE 2-7. Numerical experiments conducted by different combinations of cumulus parameterization and microphysics schemes.

Experiment	Cumulus parameterization scheme	Microphysics scheme
Model1	Kain–Fritsch (Kain and Fritsch 2004)	Kessler (Kessler 1969)
Model2	Betts–Miller–Janjic (Janjic 1994, 2000)	Kessler
Model3	Grell–Devenyi ensemble (Grell and Devenyi 2002)	Kessler
Model4	Kain–Fritsch	WSM5 (Hong et al. 2004)
Model5	Betts–Miller–Janjic	WSM5
Model6	Grell–Devenyi ensemble	WSM5

the dry static energy ($gz + c_pT$) where g is gravity and c_p the specific heat of dry air at constant pressure. The computation of Q_1 entails the calculation of the local change and the advective changes (horizontal and vertical advection) of the dry static energy. The observed counterparts of Q_1 for all these forecast time intervals are from the CSH algorithm.

First, the model- and superensemble-based forecasts of precipitation over India were validated. In Figs. 2-17a–d, the vertical bars show skill via the root-mean-square (rms) errors for the six model configurations and the superensemble for each of the forecast days. Figures 2-18a–d show the daily skill based on the area-averaged correlations of the observed and simulated rainfall. The observed rain comes from the rain gauge–based estimates of Rajeevan et al. (2008). Of interest in Figs. 2-17 and 2-18 is the slow increase in rms errors in the forecasts from day 1 to day 6 and the slow decline of the areal correlations during this forecast period. The multimodel superensemble performs the best in comparison to all of the member models in the forecast suite and exhibits very little decline in the correlations from day 1 to day 6; the rms errors of the multimodel superensemble also do not show much of an increase with forecast time. The model- and multimodel superensemble-based vertical distributions are compared with those from the CSH estimates.

Figures 2-19a–d illustrate the vertical profiles of area-averaged Q_1 (K day^{-1}) over the Indian subdomain (6.85°–25.13°N, 70°–90.17°E). These represent four

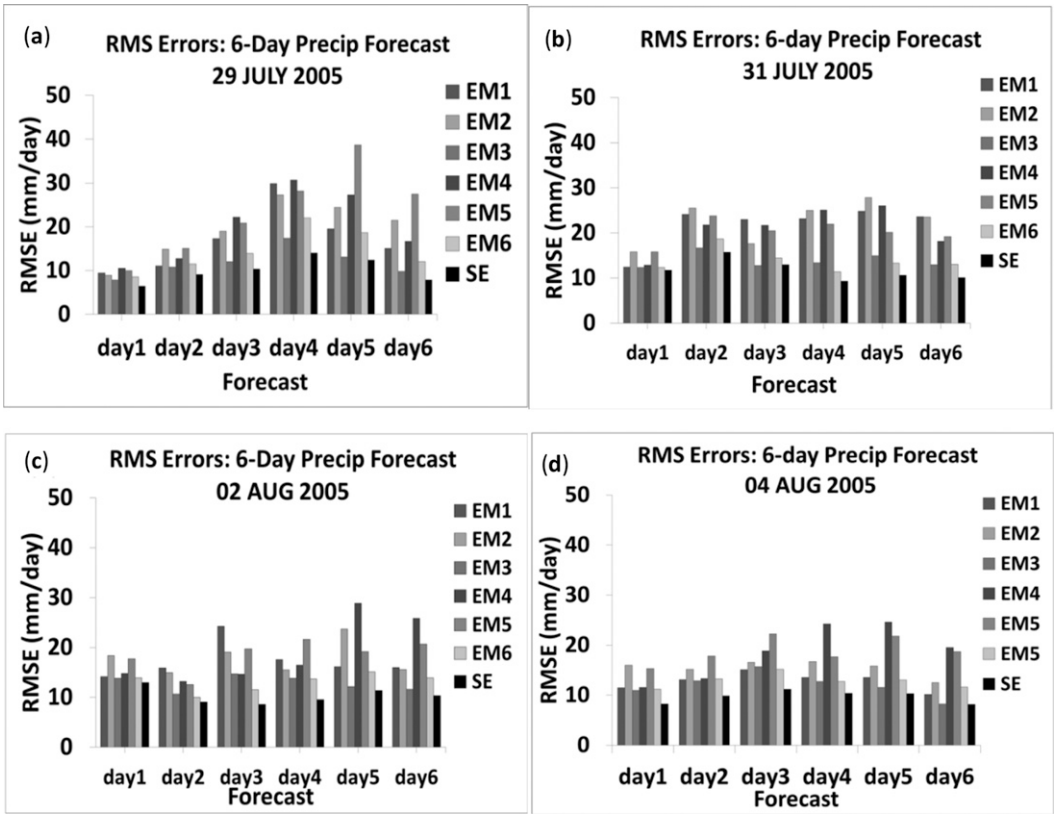

FIG. 2-17. Comparison of RMS errors for forecasts from the super ensemble and six member models over 6 days with initial conditions at **(a)** 29 July 2005, **(b)** 31 July 2005, **(c)** 2 August 2005, and **(d)** 4 August 2005.

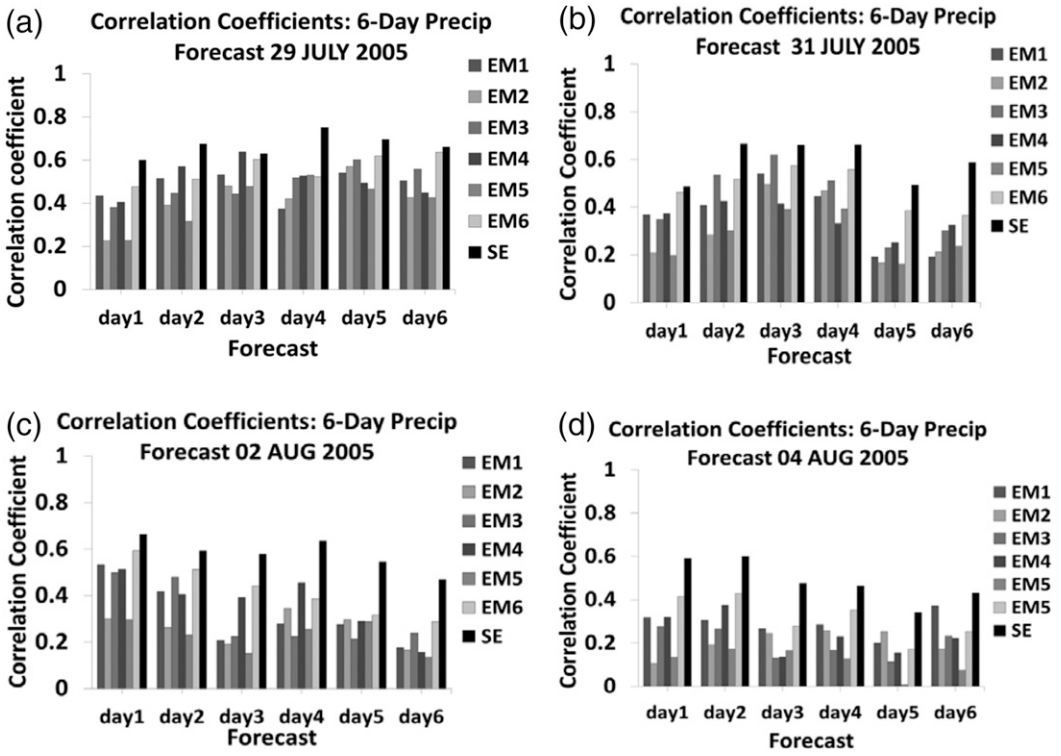

FIG. 2-18. Comparison of spatial correlation coefficients between observed and simulated rain for forecasts from the super ensemble and six member models over 6 days with initial conditions at **(a)** 29 July 2005, **(b)** 31 July 2005, **(c)** 2 August 2005, and **(d)** 4 August 2005.

selected map times during a 4-day forecast phase of the multimodel superensemble. The mesoscale models have higher values for Q_1 than do the CSH values. There are many details in the model-based profiles in the vertical. The satellite-based CSH profiles are smooth and look parabolic along the vertical as was also noted in Krishnamurti et al. (2010). The multimodel superensemble recognizes these differences between the CSH and the member model vertical profiles and removes the large differences that are persistent systematic errors. As a result the forecasts through day 4 from the multimodel superensemble come out very close to the CSH profiles. The straight ensemble mean would reside between the forecast profiles of the member models and would contain large errors. In conclusion it is safe to state that given observed measures of heating such as the CSH profiles, it is possible to produce accurate forecasts of Q_1 from the construction of a multimodel superensemble.

6. Summary and future research

a. *Summary*

This chapter presents some of the recent improvements in TRMM LH algorithms and their relationship with the pioneering works of Yanai et al. (1973). Results from an intercomparison of the LH algorithms are also presented. Differences in the derived heating profiles from the different algorithms, including their associated level of maximum heating, could be due to the physical assumptions as well as the different LUTs (i.e., CRM-simulated heating profiles used to generate the LUTs). This intercomparison will be continued in collaboration with those working on observed heating estimates, which could help to identify the salient physical processes leading to the similarities and differences produced by the retrieval algorithms. In addition, data from GPM field campaigns and ground validation sites (e.g., MC^{3}E) and others (e.g., TWP-ICE, DYNAMO[11]) that provide extensive and high-quality in situ microphysical observations will be valuable in improving and validating CRM microphysics. This is important because representative

[11] In a recent study by R. Johnson and P. Ciesielski, both CSH- and SLH-retrieved heating profiles were found to be in excellent agreement with sounding estimated heating profiles from DYNAMO. However, CSH- and SLH-retrieved LH profiles were quite different for another location over land.

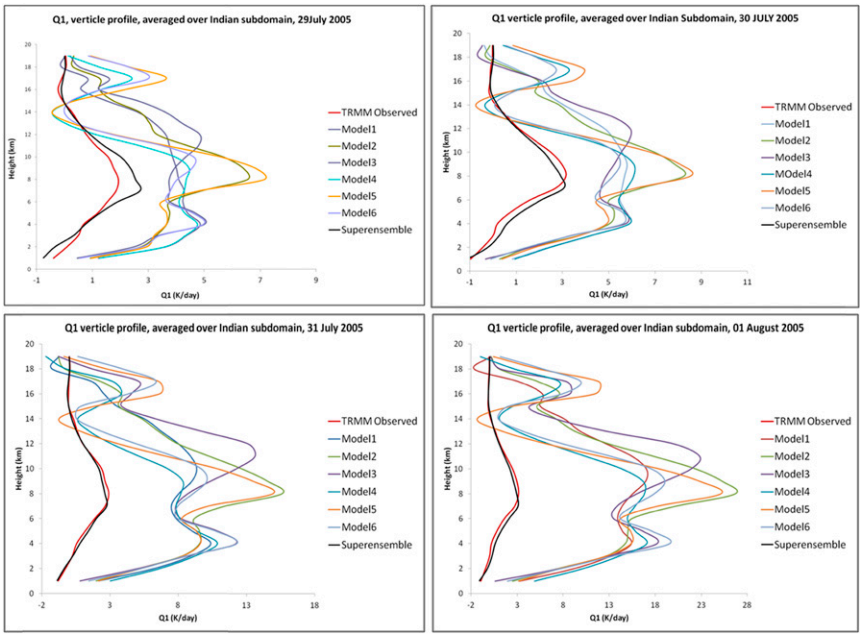

FIG. 2-19. Forecasts of the vertical distribution of heating Q_1 (K day^{-1}) from six mesoscale models, the multimodel superensemble, and the satellite-based CSH algorithm over the Indian subdomain (6.85°–25.13°N, 70°–90.17°E). The respective panels show forecasts in sequence for days 1 through 4.

microphysics is essential in reproducing, within a modeling framework, the key four-dimensional features of LH.

This paper also presented highlights published in the *Journal of Climate* special collection on TRMM diabatic heating. In particular, the comparison of heating profiles derived from TRMM LH algorithms, sounding networks, and reanalyses over the tropics were discussed. One key finding was that the major differences between the heating structures from the various estimates are related to low-level heating and the level of maximum heating. Low-level heating is important to the MJO cycle. Given the uncertainties in TRMM-based diabatic heating estimates, the central role of diabatic heating in the MJO, and the demands for reducing model deficiencies in simulating and forecasting the MJO, there is a great interest and urgent need to examine the MJO vertical heating structure and related processes in current GCMs and to explore how their structure and fidelity relate to the models' MJO representation and forecast skill. To help address these objectives, a model and observation comparison project on vertical heating structures and diabatic processes associated with the MJO is being organized through a joint effort by the WCRP–WWRP YOTC MJO Task Force and GEWEX Atmospheric System Study Project (Petch et al. 2011; www.ucar.edu/yotc/mjodiab.html).

TRMM-based LH products are also beginning to provide data assimilation guidance in numerical predictions as well as improvements in the underlying cumulus parameterization schemes. For example, these products have been used to identify the importance of the treatment of shallow convection in cumulus parameterization schemes in simulating a more realistic ITCZ. In addition, LH products have been used to improve 4-day monsoon forecasts and model physics with the construction of a multimodel superensemble.

TABLE 2-8. Summary of PMM cloud heating products from the CSH and SLH algorithms. (Orbital heating is not a standard PMM product.)

	Spatial scale	Temporal scale	Algorithm	Products
Gridded	0.5° × 0.5°, 19 vertical layers	Monthly	SLH-PR CSH-Combined	LH, $Q_1 - Q_R$, Q_2 LH, Q_1, Q_R, Q_2
Orbital	Pixel, 19 vertical layers	Instantaneous	SLH-PR CSH-Combined	LH, $Q_1 - Q_R$, Q_2 LH, Q_1, Q_R, Q_2
Gridded orbital	0.5° × 0.5°, 19 vertical layers	Instantaneous with time stamps on each grid	SLH-PR CSH-Combined	LH, $Q_1 - Q_R$, Q_2 LH, Q_1, Q_R, Q_2

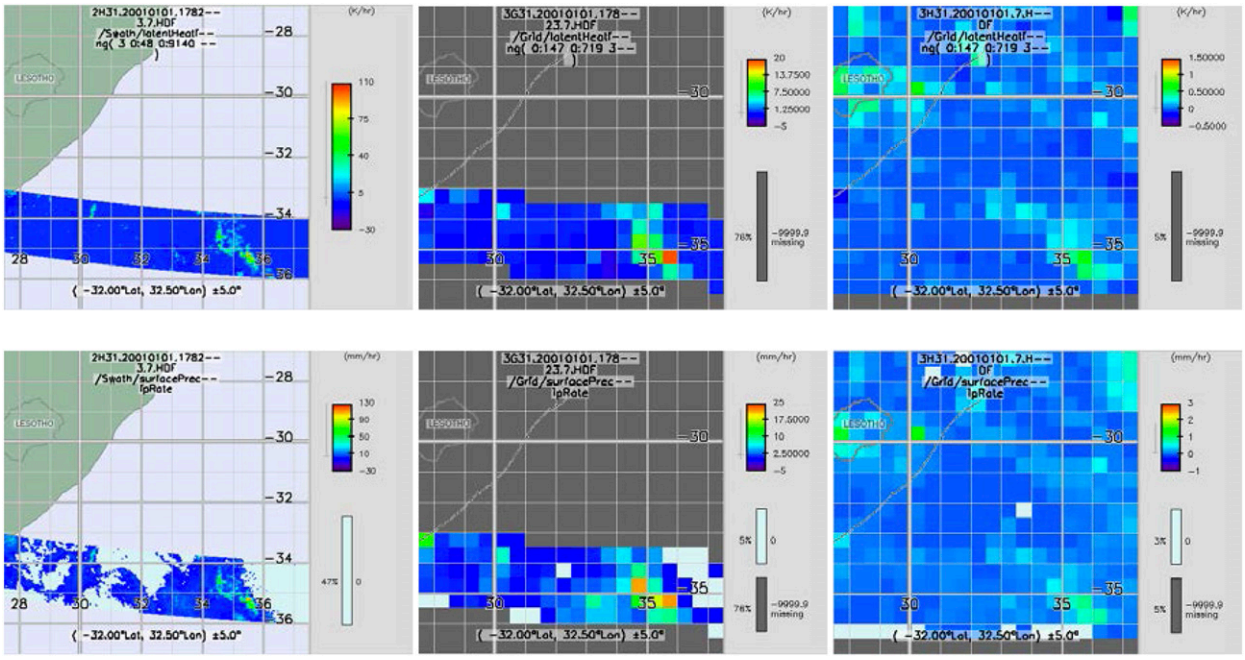

FIG. 2-20. LH products from the version 2 CSH algorithm based on rainfall data from the TRMM combined algorithm: (left) instantaneous pixel scale LH off the southeast coast of Africa 1 Jan 2001 at a height near 2.5 km from the orbital product, (center) same but for the 3G31 gridded (0.5° × 0.5°) orbital product, and (right) same but for monthly mean LH from the 3H31 gridded monthly product. The new CSH algorithm uses conditional rain rates and LUTs based on GCE results divided into fine intensity and stratiform bins (Tao et al. 2010). The corresponding surface rainfall is shown below each of the LH products.

b. *Standard LH products*

The PMM joint science team has decided to have two standard LH algorithms: the Goddard CSH algorithm and the SLH algorithm. Table 2-8 lists the required data and type of heating products for these two algorithms. Note that one of the major inputs for these standard products is the improved rainfall estimate. Figure 2-20 shows an example of the LH products generated from the new version of the CSH algorithm.

Standard LH products from TRMM will represent a valuable new source of data for the research community, products that, a decade ago, were considered beyond reach. These data products will enable compelling new investigations into the complexities of storm life cycles, diabatic heating controls, and feedbacks related to mesoscale and synoptic-scale circulations and the influence of diabatic heating on Earth's general circulation and climate. In particular, the LH estimates will be of great help as a benchmark for a model intercomparison study on vertical MJO heating structures as shown in section 5b and for the model intercomparison experiment mentioned above. The standard LH products could help to determine how well the model-simulated heating structures agree with observations and determine how different they are relative to the spread of observational (reanalysis and TRMM) values, which would also address the question of how useful the observations are at this point.

c. *Future directions*

Since temperature (heating) and water vapor (moistening/drying) are closely related (Yanai et al. 1973), it is proposed to produce both heating and moistening profiles using GPM rainfall products. Both LH and moistening profiles are also needed for improving large-scale model simulations and forecasts (Rajendran et al. 2004). GPM will produce higher temporal (3-hourly) and spatial resolution (up to 0.05°) rainfall products. Several issues therefore need to be addressed. CRM results have shown that the horizontal eddy term is quite small if averaged over a large area. In addition, the CRM results have indicated that the horizontal and vertical eddy transport terms usually counteract each other (mass continuity) over small spatial scales (cloud scales). The contribution by horizontal and vertical eddy heat and moisture transport to the heat and moisture budgets must be examined at various horizontal resolutions (e.g., TRMM and GPM satellite footprint sizes). It may be necessary to produce heating and moistening profiles including all of the eddy transport and microphysics terms. Also, the accuracy of the heating retrievals could be affected by differences in the convective–stratiform separation. As

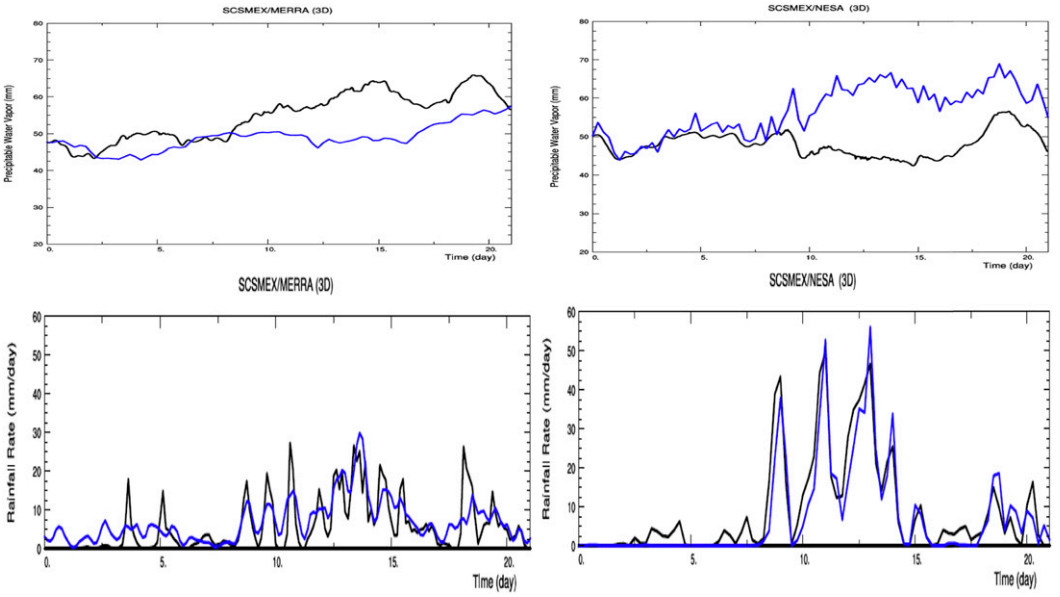

FIG. 2-21. Time series of simulated and observed (top) precipitable water and (bottom) precipitation rate using forcing derived from MERRA. The black lines are model-simulated, and the blue lines are observed. The left panels depict MERRA-forced simulations, and the right panels depict simulations using forcing derived from soundings during SCSMEX (NESA).

such, the separation algorithms used in the LH algorithms should be as close as possible to those applied to the satellite data and at a comparable scale but this is likely only a secondary issue with regard to the current standard algorithms, as their separation schemes are fairly close to the satellite's.

Only a limited number of CRM-simulated cases were used to build the SLH and CSH algorithm (see section 3) LUTs. Observations from additional field experiments (e.g., TWP-ICE, MC^{3}E, DYNAMO) and future GV site(s) will be needed to provide new types of initial conditions to CRMs to expand the number of cases and environments represented in the LUTs. In addition, large-scale reanalysis products such as MERRA can be used both to improve cloud-resolving simulations by placing them in a larger-scale dynamical context and to expand the range of environmental conditions explored by CRM simulations beyond field experiments. Figure 2-21 depicts preliminary results comparing simulations forced by the SCSMEX sounding network versus simulations forced by MERRA on GCE grid boundaries in the same location. The rainfall and precipitable water amounts obtained from simulations forced by MERRA agree with the MERRA values themselves at least as well as (and even better with regard to precipitable water) those obtained from simulations forced by the sounding network do with those from the sounding budget itself. This suggests that the GCE-MERRA approach has the potential to provide reasonably good-quality simulations to the heating algorithms for a variety of locations and conditions, including those regions with large surface rainfall, such as the Indian Ocean, SPCZ, South America, Africa, and snow events, which are not well represented in the current LUTs. In addition to expanding the number and type of environments, further improvements to the CSH LUTs will be made by using the improved and validated physics in the GCE and running cases at higher resolution. The GCE+MERRA simulated cloud datasets in the Cloud Data Library (http://cloud.gsfc.nasa.gov) can be used to improve the performance of satellite-based rainfall and LH retrievals through more representative LUTs and to improve moist process parameterizations for GCMs.

Acknowledgments. The authors extend their heartfelt appreciation to the late Professor Michio Yanai of the University of California at Los Angeles. The enthusiasm of Dr. Yanai over the years and his willingness to discuss ideas concerning the subject of atmospheric latent heating and its implications with the various authors has had a profound influence on ideas central to this paper. We also appreciate the leadership of the late Dr. Joanne Simpson, a close colleague of Dr. Yanai and the first TRMM project scientist in the United States, and the late Prof. Tsuyoshi Nitta, who was a student of Dr. Yanai and the TRMM project scientist in Japan. Drs. Simpson, Robert Adler, Robert Houze, and Nitta promoted LH as being one of the two key products for TRMM. The authors also

thank two anonymous reviewers for their constructive comments that improved this paper considerably.

Acknowledgment is also made to the NASA Center for Climate Simulation (NCCS) at the NASA Goddard Space Flight Center for computer time used in this research. Finally, the authors appreciate the implementation of LH retrieval algorithms into the Precipitation Processing System also at the NASA Goddard Space Flight Center and the TRMM Mission Operation System at the Japan Aerospace Exploration Agency (JAXA) for the production of standardized LH products. This research has been supported by an assortment of PMM Science Team grants under the auspices of both the National Aeronautics and Space Administration (NASA) and the Japan Aerospace Exploration Agency (JAXA). D. Waliser's contribution was carried out on behalf of the Jet Propulsion Laboratory, California Institute of Technology, under a contract with NASA. X. Jiang was also supported by the NSF Climate and Large-Scale Dynamics Program under Awards ATM-0934285 and AGS-1228302.

APPENDIX

Definitions of Acronyms

AMIE	ARM MJO Investigation Experiment
AMMA	African Monsoon Multidisciplinary Analysis
AORI	Atmosphere and Ocean Research Institute
ARM	Atmospheric Radiation Measurement
ARW	Advanced Research WRF
CFADs	Contoured frequency with altitude diagrams
CFSR	NCEP Climate Forecast System Reanalyses
CISK	Conditional instability of the second kind
CMIP3	Coupled Model Intercomparison Project phase 3
CRM	Cloud-resolving model
CSH	Convective–stratiform heating
DIAG	Sounding-diagnosed
DOE	Department of Energy
DYNAMO	Dynamics of the MJO
EBBR	Energy balance Bowen ratio
ECMWF	European Centre for Medium-Range Weather Forecasts
EEIO	Eastern equatorial Indian Ocean
EMEX	Equatorial Monsoon Experiment
EOF	Empirical orthogonal function
ERA-40	40-Year ECMWF Re-Analysis
ERA-I	ECMWF interim reanalysis
ETH	Echo-top height
GATE	Global Atmospheric Research Program (GARP) Atlantic Tropical Experiment
GCE	Goddard Cumulus Ensemble model
GCM	General circulation model
GPM	Global precipitation measurement
GPROF	Goddard profiling algorithm
GV	Ground validation
HERB	Hydrologic cycle and Earth Radiation Budget
HH	Hydrometeor heating
IFA	Intensive flux array
ITCZ	Intertropical convergence zone
JAMSTEC	Japan Agency for Marine-Earth Science and Technology
JAXA	Japan Aerospace Exploration Agency
JRA-25	Japanese 25-Year Reanalysis
KWAJEX	Kwajalein Experiment
LBA	Large-Scale Biosphere–Atmosphere Experiment
LH	Latent heating
LUT	Lookup table
MC^3E	Midlatitude Continental Convective Clouds Experiment
MIROC5	Model for Interdisciplinary Research on Climate, version 5
MCS	Mesoscale convective system
MERRA	Modern-Era Retrospective Analysis for Research and Applications
MISMO	Mirai Indian Ocean Cruise for the Study of the MJO Convection Onset
MJO	Madden–Julian oscillation
NASA	National Aeronautics and Space Administration
NCEP-FNL	NCEP Global Forecast System (GFS) final
NCEP	National Centers for Environmental Prediction
NCEP-2	NCEP–Department of Energy (DOE) reanalysis
NESA	Northern enhanced sounding array
NIES	National Institute for Environmental Studies
NOAA	National Oceanographic and Atmospheric Administration
NOAH	NCEP–Oregon State University (Dept. of Atmospheric Sciences)/Air Force/Hydrologic Research Laboratory (Office of Hydrologic Development)
OREOF	Oblique rotated EOF
PBL	Planetary boundary layer
PDF	Probability distribution function
PRH	Precipitation radar heating
PRE-STORM	Preliminary Regional Experiment for STORM-Central
PMW	Passive microwave

PR	Precipitation Radar
PTH	Precipitation top height
Q_1	Apparent heat source
Q_2	Apparent moisture sink
Q_R	Radiation
rms	root-mean-square
RRTM	Rapid Radiative Transfer Model
SCSMEX	South China Sea Monsoon Experiment
SESA	Southern enhanced sounding array
SGP	Southern Great Plains
SLH	Spectral latent heating
SPCZ	South Pacific convergence zone
SST	Sea surface temperature
TMI	TRMM Microwave Imager
TOGA COARE	Tropical Ocean Global Atmosphere–Coupled Ocean–Atmosphere Response Experiment
TRAIN	Trained radiometer
TRMM	Tropical Rainfall Measuring Mission
TWP-ICE	Tropical Warm Pool–International Cloud Experiment
WCRP	World Climate Research Program
WH index	Wheeler–Hendon index
WP	Western Pacific
WRF	Weather Research and Forecasting Model
WWRP	World Weather Research Program
VIRS	Visible and Infrared Scanner
YOTC	Year of Tropical Convection

REFERENCES

Ackerman, T. P., and G. M. Stokes, 2003: The Atmospheric Radiation Measurement Program. *Phys. Today*, **56**, 38–44, doi:10.1063/1.1554135.

Benedict, J. J., and D. A. Randall, 2009: Structure of the Madden–Julian oscillation in the superparameterized CAM. *J. Atmos. Sci.*, **66**, 3277–3296, doi:10.1175/2009JAS3030.1.

Bretherton, C., M. E. Peters, and L. E. Back, 2004: Relationships between water vapor path and precipitation over the tropical oceans. *J. Climate*, **17**, 1517–1528, doi:10.1175/1520-0442(2004)017<1517:RBWVPA>2.0.CO;2.

Chikira, M., and M. Sugiyama, 2010: A cumulus parameterization with state-dependent entrainment rate. Part I: Description and sensitivity to temperature and humidity profiles. *J. Atmos. Sci.*, **67**, 2171–2193, doi:10.1175/2010JAS3316.1.

Ciesielski, P. E., and R. H. Johnson, 2006: Contrasting characteristics of convection over the northern and southern South China Sea during SCSMEX. *Mon. Wea. Rev.*, **134**, 1041–1062, doi:10.1175/MWR3113.1.

——, ——, P. T. Haertel, and J. Wang, 2003: Corrected TOGA COARE sounding humidity data: Impact on diagnosed properties of convection and climate over the warm pool. *J. Climate*, **16**, 2370–2384, doi:10.1175/2790.1.

Del Genio, A. D., Y.-H. Chen, D.-H. Kim, and M.-S. Yao, 2012: The MJO transition from shallow to deep convection in *CloudSat*/CALIPSO data and GISS GCM simulations. *J. Climate*, **25**, 3755–3770, doi:10.1175/JCLI-D-11-00384.1.

Fairall, C., E. F. Bradley, D. P. Rogers, J. B. Edson, and G. S. Young, 1996: Bulk parameterization of air–sea fluxes for Tropical Ocean–Global Atmosphere Coupled–Ocean Atmosphere Response Experiment. *J. Geophys. Res.*, **101**, 3747–3764, doi:10.1029/95JC03205.

Fu, X. H., and B. Wang, 2009: Critical roles of the stratiform rainfall in sustaining the Madden–Julian oscillation: GCM experiments. *J. Climate*, **22**, 3939–3959, doi:10.1175/2009JCLI2610.1.

Gamache, J. F., and R. A. Houze Jr., 1983: Water budget of a mesoscale convective system in the tropics. *J. Atmos. Sci.*, **40**, 1835–1850, doi:10.1175/1520-0469(1983)040<1835:WBOAMC>2.0.CO;2.

Grecu, M., and W. S. Olson, 2006: Bayesian estimation of precipitation from satellite passive microwave observations using combined radar–radiometer retrievals. *J. Appl. Meteor. Climatol.*, **45**, 416–433, doi:10.1175/JAM2360.1.

——, ——, C.-L. Shie, T. L'Ecuyer, and W.-K. Tao, 2009: Combining satellite microwave radiometer and radar observations to estimate atmospheric latent heating profiles. *J. Climate*, **22**, 6356–6376, doi:10.1175/2009JCLI3020.1.

Grell, G. A., and D. Devenyi, 2002: A generalized approach to parameterizing convection combining ensemble and data assimilation techniques. *Geophys. Res. Lett.*, **29**, 1693, doi:10.1029/2002GL015311.

Hagos, S., and Coauthors, 2010: Estimates of tropical diabatic heating profiles: Commonalities and uncertainties. *J. Climate*, **23**, 542–558, doi:10.1175/2009JCLI3025.1.

Hirota, N., Y. N. Takayabu, M. Watanabe, and M. Kimoto, 2011: Precipitation reproducibility over tropical oceans and its relationship to the double ITCZ problem in CMIP3 and MIROC5 climate models. *J. Climate*, **24**, 4859–4873, doi:10.1175/2011JCLI4156.1.

——, ——, ——, ——, and M. Chikira, 2014: Role of convective entrainment in spatial distributions of and temporal variations in precipitation over tropical oceans. *J. Climate*, **27**, 8707–8723, doi:10.1175/JCLI-D-13-00701.1.

Hong, S.-Y., J. Dudhia, and S.-H. Chen, 2004: A revised approach to ice microphysical processes for the bulk parameterization of clouds and precipitation. *Mon. Wea. Rev.*, **132**, 103–120, doi:10.1175/1520-0493(2004)132<0103:ARATIM>2.0.CO;2.

Houze, R. A., Jr., 1982: Cloud clusters and large-scale vertical motions in the tropics. *J. Meteor. Soc. Japan*, **60**, 396–409.

——, 1989: Observed structure of mesoscale convective systems and implications for large-scale heating. *Quart. J. Roy. Meteor. Soc.*, **115**, 425–461, doi:10.1002/qj.49711548702.

——, 1997: Stratiform precipitation in regions of convection: A meteorological paradox? *Bull. Amer. Meteor. Soc.*, **78**, 2179–2196, doi:10.1175/1520-0477(1997)078<2179:SPIROC>2.0.CO;2.

——, and A. K. Betts, 1981: Convection in GATE. *Rev. Geophys.*, **19**, 541–576, doi:10.1029/RG019i004p00541.

Jakob, C., and C. Schumacher, 2008: Precipitation and latent heating characteristics of the major tropical western Pacific cloud regimes. *J. Climate*, **21**, 4348–4364, doi:10.1175/2008JCLI2122.1.

Janjic, Z. I., 1994: The step-mountain eta coordinate model: Further developments of the convection, viscous sublayer and turbulence closure schemes. *Mon. Wea. Rev.*, **122**, 927–945, doi:10.1175/1520-0493(1994)122<0927:TSMECM>2.0.CO;2.

——, 2000: Comments on ''Development and evaluation of a convection scheme for use in climate models.'' *J. Atmos.*

Sci., **57**, 3686, doi:10.1175/1520-0469(2000)057<3686:CODAEO>2.0.CO;2.

Jiang, X., and Coauthors, 2009: Vertical heating structures associated with the MJO as characterized by TRMM estimates, ECMWF reanalyses, and forecasts: A case study during 1998/99 winter. *J. Climate*, **22**, 6001–6020, doi:10.1175/2009JCLI3048.1.

——, and Coauthors, 2011: Vertical diabatic heating structure of the MJO: Intercomparison between recent reanalyses and TRMM estimates. *Mon. Wea. Rev.*, **139**, 3208–3223, doi:10.1175/2011MWR3636.1.

Johnson, R. H., 1984: Partitioning tropical heat and moisture budgets into cumulus and mesoscale components: Implications for cumulus parameterization. *Mon. Wea. Rev.*, **112**, 1590–1601, doi:10.1175/1520-0493(1984)112<1590:PTHAMB>2.0.CO;2.

——, and P. J. Hamilton, 1988: The relationship of surface pressure features to the precipitation and airflow structure of an intense mid-latitude squall line. *Mon. Wea. Rev.*, **116**, 1444–1473, doi:10.1175/1520-0493(1988)116<1444:TROSPF>2.0.CO;2.

——, and P. E. Ciesielski, 2002: Characteristics of the 1998 summer monsoon onset over the northern South China Sea. *J. Meteor. Soc. Japan*, **80**, 561–578, doi:10.2151/jmsj.80.561.

Kain, J. S., and M. Fritsch, 2004: The Kain–Fritsch convective parameterization: An update. *J. Appl. Meteor.*, **43**, 170–181, doi:10.1175/1520-0450(2004)043<0170:TKCPAU>2.0.CO;2.

Katsumata, M., R. H. Johnson, and P. E. Ciesielski, 2009: Observed synoptic-scale variability during the developing phase of an ISO over the Indian Ocean during MISMO. *J. Atmos. Sci.*, **66**, 3434–3448, doi:10.1175/2009JAS3003.1.

Kessler, E., 1969: *On the Distribution and Continuity of Water Substance in Atmospheric Circulation*, *Meteor. Monogr.*, No. 32, Amer. Meteor. Soc., 84 pp.

Kiladis, G. N., K. H. Straub, and P. T. Haertel, 2005: Zonal and vertical structure of the Madden–Julian oscillation. *J. Atmos. Sci.*, **62**, 2790–2809, doi:10.1175/JAS3520.1.

Kim, D., and Coauthors, 2009: Application of MJO simulation diagnostics to climate models. *J. Climate*, **22**, 6413–6436, doi:10.1175/2009JCLI3063.1.

Krishnamurti, T. N., C. M. Kishtawal, W. D. Shin, and C. E. Williford, 2000a: Improving tropical precipitation forecasts from a multianalysis superensemble. *J. Climate*, **13**, 4217–4227, doi:10.1175/1520-0442(2000)013<4217:ITPFFA>2.0.CO;2.

——, ——, Z. Zhang, T. Larow, D. Bachiochi, E. Williford, S. Gadgil, and S. Surendran, 2000b: Multimodel ensemble forecasts for weather and seasonal climate. *J. Climate*, **13**, 4196–4216, doi:10.1175/1520-0442(2000)013<4196:MEFFWA>2.0.CO;2.

——, C. Gnanaseelan, and A. Chakraborty, 2007: Prediction of the diurnal cycle using a multimodel superensemble. Part I: Precipitation. *Mon. Wea. Rev.*, **135**, 3613–3632, doi:10.1175/MWR3446.1.

——, A. Chakraborty, and A. K. Mishra, 2010: Improving multimodel forecasts of the vertical distribution of heating using the TRMM profiles. *J. Climate*, **23**, 1079–1094, doi:10.1175/2009JCLI2878.1.

——, A. Simon, A. Thomas, A. Mishra, D. Sikka, D. Niyogi, A. Chakraborty, and L. Li, 2012: Modeling of forecast sensitivity on the march of monsoon isochrones from Kerala to New Delhi: The first 25 days. *J. Atmos. Sci.*, **69**, 2465–2487, doi:10.1175/JAS-D-11-0170.1.

Krueger, S. K., 1988: Numerical simulation of tropical cumulus clouds and their interaction with the subcloud layer. *J. Atmos. Sci.*, **45**, 2221–2250, doi:10.1175/1520-0469(1988)045<2221:NSOTCC>2.0.CO;2.

Kummerow, C., W. Barnes, T. Kozu, J. Shiue, and J. Simpson, 1998: The Tropical Rainfall Measurement Mission (TRMM) sensor package. *J. Atmos. Oceanic Technol.*, **15**, 809–817, doi:10.1175/1520-0426(1998)015<0809:TTRMMT>2.0.CO;2.

Lang, S., W.-K. Tao, R. Cifelli, W. Olson, J. Halverson, S. Rutledge, and J. Simpson, 2007: Improving simulations of convective system from TRMM LBA: Easterly and westerly regimes. *J. Atmos. Sci.*, **64**, 1141–1164, doi:10.1175/JAS3879.1.

——, ——, and X. Zeng, 2011: Reducing the biases in simulated radar reflectivities from a bulk microphysics scheme: Tropical convective systems. *J. Atmos. Sci.*, **68**, 2306–2320, doi:10.1175/JAS-D-10-05000.1.

Lau, K.-M., and Coauthors, 2000: A report of the field operations and early results of the South China Sea Monsoon Experiment (SCSMEX). *Bull. Amer. Meteor. Soc.*, **81**, 1261–1270, doi:10.1175/1520-0477(2000)081<1261:AROTFO>2.3.CO;2.

Lau, W. K.-M., and H.-T. Wu, 2010: Characteristics of precipitation, cloud, and latent heating associated with the Madden–Julian oscillation. *J. Climate*, **23**, 504–518, doi:10.1175/2009JCLI2920.1.

——, and D. E. Waliser, 2011: *Intraseasonal Variability in the Atmosphere–Ocean Climate System.* 2nd ed. Springer, 613 pp.

L'Ecuyer, T. S., and G. L. Stephens, 2003: The tropical oceanic energy budget from the TRMM perspective. Part I: Algorithm and uncertainties. *J. Climate*, **16**, 1967–1985, doi:10.1175/1520-0442(2003)016<1967:TTOEBF>2.0.CO;2.

——, and ——, 2007: The tropical atmospheric energy budget from the TRMM perspective. Part II: Evaluating GCM representations of the sensitivity of regional energy and water cycles to the 1998–99 ENSO cycle. *J. Climate*, **20**, 4548–4571, doi:10.1175/JCLI4207.1.

Lee, M.-I., I.-S. Kang, J.-K. Kim, and B. E. Mapes, 2001: Influence of cloud–radiation interaction on simulating tropical intraseasonal oscillation with an atmospheric general circulation model. *J. Geophys. Res.*, **106**, 14 219–14 233, doi:10.1029/2001JD900143.

Li, C., X. Jia, J. Ling, W. Zhou, and C. Zhang, 2009: Sensitivity of MJO simulations to diabatic heating profiles. *Climate Dyn.*, **32**, 167–187, doi:10.1007/s00382-008-0455-x.

Li, X., C.-H. Sui, K.-M. Lau, and M.-D. Chou, 1999: Large-scale forcing and cloud–radiation interaction in the tropical deep convective regime. *J. Atmos. Sci.*, **56**, 3028–3042, doi:10.1175/1520-0469(1999)056<3028:LSFACR>2.0.CO;2.

Lin, J., B. E. Mapes, M. Zhang, and M. Newman, 2004: Stratiform precipitation, vertical heating profiles, and the Madden–Julian oscillation. *J. Atmos. Sci.*, **61**, 296–309, doi:10.1175/1520-0469(2004)061<0296:SPVHPA>2.0.CO;2.

——, and Coauthors, 2006: Tropical intraseasonal variability in 14 IPCC AR4 climate models. Part I: Convective signals. *J. Climate*, **19**, 2665–2690, doi:10.1175/JCLI3735.1.

Lin, X., and R. H. Johnson, 1996: Heating, moistening, and rainfall over the western Pacific during TOGA COARE. *J. Atmos. Sci.*, **53**, 3367–3383, doi:10.1175/1520-0469(1996)053<3367:HMAROT>2.0.CO;2.

Ling, J., and C. Zhang, 2011: Structural evolution in heating profiles of the MJO in global reanalyses and TRMM retrievals. *J. Climate*, **24**, 825–842, doi:10.1175/2010JCLI3826.1.

——, and ——, 2013: Diabatic heating profiles in recent global reanalyses. *J. Climate*, **26**, 3307–3325, doi:10.1175/JCLI-D-12-00384.1.

Mapes, B. E., and R. A. Houze Jr., 1995: Diabatic divergence profiles in western Pacific mesoscale convective systems. *J. Atmos. Sci.*, **52**, 1807–1828, doi:10.1175/1520-0469(1995)052<1807:DDPIWP>2.0.CO;2.

Masunaga, H., T. S. L'Ecuyer, and C. D. Kummerow, 2005: Variability in the characteristics of precipitation systems in the tropical Pacific. Part I: Spatial structure. *J. Climate*, **18**, 823–840, doi:10.1175/JCLI-3304.1.

Mather J. H., S. A. McFarlane, M. Miller, and K. L. Johnson, 2007: Cloud properties and associated radiative heating rates in the tropical western Pacific. *J. Geophys. Res.*, **112**, D05201, doi:10.1029/2006JD007555.

May, P. T., J. H. Mather, G. Vaughan, C. Jakob, G. M. McFarquar, and G. G. Mace, 2008: The Tropical Warm Pool International Cloud Experiment. *Bull. Amer. Meteor. Soc.*, **89**, 629–645, doi:10.1175/BAMS-89-5-629.

Moncrieff, M. W., S. K. Krueger, D. Gregory, J.-L. Redelsperger, and W.-K. Tao, 1997: GEWEX Cloud System Study (GCSS) Working Group 4: Precipitating convective cloud systems. *Bull. Amer. Meteor. Soc.*, **78**, 831–845, doi:10.1175/1520-0477(1997)078<0831:GCSSGW>2.0.CO;2.

Morita, J., Y. N. Takayabu, S. Shige, and Y. Kodama, 2006: Analysis of rainfall characteristics of the Madden–Julian oscillation using TRMM satellite data. *Dyn. Atmos. Oceans*, **42**, 107–126, doi:10.1016/j.dynatmoce.2006.02.002.

Olson, W. S., C. D. Kummerow, Y. Hong, and W.-K. Tao, 1999: Atmospheric latent heating distributions in the tropics derived from satellite passive microwave radiometer measurements. *J. Appl. Meteor.*, **38**, 633–664, doi:10.1175/1520-0450(1999)038<0633:ALHDIT>2.0.CO;2.

——, and Coauthors, 2006: Precipitation and latent heating distributions from satellite passive microwave radiometry. Part I: Improved method and uncertainties. *J. Appl. Meteor.*, **45**, 702–720, doi:10.1175/JAM2369.1.

Petch, J., D. Waliser, X. Jiang, P. Xavier, and S. Woolnough, 2011: A global model inter-comparison of the physical processes associated with the MJO. *GEWEX News*, No. 21, International GEWEX Project Office, Silver Spring, MD, 3–5.

Rajeevan, M., J. Bhate, and A. K. Jaswal, 2008: Analysis of variability and trends of extreme rainfall events over India using 104 years of gridded daily rainfall data. *Geophys. Res. Lett.*, **35**, L18707, doi:10.1029/2008GL035143.

Rajendran, R., T. N. Krishnamurti, V. Misra, and W.-K. Tao, 2004: An empirical cumulus parameterization scheme based on TRMM latent heating profiles. *J. Meteor. Soc. Japan*, **82**, 989–1006.

Randall, D., and Coauthors, 2003: Confronting models with data: The GEWEX Cloud Systems Study. *Bull. Amer. Meteor. Soc.*, **84**, 455–469, doi:10.1175/BAMS-84-4-455.

Raymond, D. J., 2001: A new model of the Madden–Julian oscillation. *J. Atmos. Sci.*, **58**, 2807–2819, doi:10.1175/1520-0469(2001)058<2807:ANMOTM>2.0.CO;2.

Rodgers, E. B., W. S. Olson, V. M. Karyampudi, and H. F. Pierce, 1998: Satellite-derived latent heating distribution and environmental influences in Hurricane Opal (1995). *Mon. Wea. Rev.*, **126**, 1229–1247, doi:10.1175/1520-0493(1998)126<1229:SDLHDA>2.0.CO;2.

——, ——, J. Halverson, J. Simpson, and H. Pierce, 2000: Environmental forcing of Supertyphoon Paka's (1997) latent heat structure. *J. Appl. Meteor.*, **39**, 1983–2006, doi:10.1175/1520-0450(2001)040<1983:EFOSPS>2.0.CO;2.

Rutledge, S. A., and R. A. Houze Jr., 1987: A diagnostic modeling study of the trailing stratiform rain of a midlatitude squall line. *J. Atmos. Sci.*, **44**, 2640–2656, doi:10.1175/1520-0469(1987)044<2640:ADMSOT>2.0.CO;2.

Satoh, S., and A. Noda, 2001: Retrieval of latent heating profiles from TRMM radar data. *Proc. 30th Int. Conf. on Radar Meteorology*, Munich, Germany, Amer. Meteor. Soc., 340–342.

Schumacher, C., M. H. Zhang, and P. E. Ciesielski, 2007: Heating structures of the TRMM field campaigns. *J. Atmos. Sci.*, **64**, 2593–2610, doi:10.1175/JAS3938.1.

Seo, K.-H., and W. Wang, 2010: The Madden–Julian oscillation simulated in the NCEP Climate Forecast System Model: The importance of stratiform heating. *J. Climate*, **23**, 4770–4793, doi:10.1175/2010JCLI2983.1.

Sherwood, S. C., 1999: Convective precursors and predictability in the tropical western Pacific. *Mon. Wea. Rev.*, **127**, 2977–2991, doi:10.1175/1520-0493(1999)127<2977:CPAPIT>2.0.CO;2.

Shige, S., Y. N. Takayabu, W.-K. Tao, and D. E. Johnson, 2004: Spectral retrieval of latent heating profiles from TRMM PR data. Part I: Development of a model-based algorithm. *J. Appl. Meteor.*, **43**, 1095–1113, doi:10.1175/1520-0450(2004)043<1095:SROLHP>2.0.CO;2.

——, ——, ——, and C.-L. Shie, 2007: Spectral retrieval of latent heating profiles from TRMM PR data. Part II: Algorithm improvement and heating estimates over tropical ocean regions. *J. Appl. Meteor. Climatol.*, **46**, 1098–1124, doi:10.1175/JAM2510.1.

——, ——, and ——, 2008: Spectral retrieval of latent heating profiles from TRMM PR data. Part III: Moistening estimates over the tropical ocean regions. *J. Appl. Meteor. Climatol.*, **47**, 620–640, doi:10.1175/2007JAMC1738.1.

——, ——, S. Kida, W.-K. Tao, X. Zeng, C. Yokoyama, and T. L'Ecuyer, 2009: Spectral retrieved of latent heating profiles from TRMM PR data. Part VI: Comparisons of lookup tables from two- and three-dimensional simulations. *J. Climate*, **22**, 5577–5594, doi:10.1175/2009JCLI2919.1.

——, S. Kida, H. Ashiwake, T. Kubota, and K. Aonashi, 2013: Improvement of TMI rain retrievals in mountainous areas. *J. Appl. Meteor. Climatol.*, **52**, 242–254, doi:10.1175/JAMC-D-12-074.1.

Short, D. A., and K. Nakamura, 2000: TRMM radar observations of shallow precipitation over the tropical oceans. *J. Climate*, **13**, 4107–4124, doi:10.1175/1520-0442(2000)013<4107:TROOSP>2.0.CO;2.

Silva Dias, M., and Coauthors, 2002: Cloud and rain processes in a biosphere–atmosphere interaction context in the Amazon region. *J. Geophys. Res.*, **107**, 8072, doi:10.1029/2001JD000335.

Slingo, J. M., P. M. Inness, and K. R. Sperber, 2005: Modeling. *Intraseasonal Variability in the Atmosphere–Ocean Climate System*, W. K. M. Lau and D. E. Waliser, Eds., Springer, 361–388.

Sobel, A. H., and H. Gildor, 2003: A simple time-dependent model of SST hot spots. *J. Climate*, **16**, 3978–3992, doi:10.1175/1520-0442(2003)016<3978:ASTMOS>2.0.CO;2.

Soong, S.-T., and W.-K. Tao, 1980: Response of deep tropical clouds to mesoscale processes. *J. Atmos. Sci.*, **37**, 2016–2034, doi:10.1175/1520-0469(1980)037<2016:RODTCC>2.0.CO;2.

Sui, C.-H., and M. Yanai, 1986: Cumulus ensemble effects on the large-scale vorticity and momentum fields of GATE. Part I: Observational evidence. *J. Atmos. Sci.*, **43**, 1618–1642, doi:10.1175/1520-0469(1986)043<1618:CEEOTL>2.0.CO;2.

Takayabu, Y. N., 2002: Spectral representation of rain features and diurnal variations observed with TRMM PR over the equatorial areas. *Geophys. Res. Lett.*, **29**, 301–304, doi:10.1029/2001GL014113.

——, K.-M. Lau, and C.-H. Sui, 1996: Observation of a quasi-2-day wave during TOGA COARE. *Mon. Wea. Rev.*, **124**, 1892–1913, doi:10.1175/1520-0493(1996)124<1892:OOAQDW>2.0.CO;2.

——, J. Yokomori, and K. Yoneyama, 2006: A diagnostic study on interactions between atmospheric thermodynamic structure

and cumulus convection over the tropical western Pacific Ocean and over the Indochina Peninsula. *J. Meteor. Soc. Japan*, **84A**, 151–169, doi:10.2151/jmsj.84A.151.

——, S. Shige, W.-K. Tao, and N. Hirota, 2010: Shallow and deep latent heating modes over tropical oceans observed with TRMM PR spectral latent heating data. *J. Climate*, **23**, 2030–2046, doi:10.1175/2009JCLI3110.1.

Takemi, T., O. Hirayama, and C. Liu, 2004: Factors responsible for the vertical development of tropical oceanic cumulus convection. *Geophys. Res. Lett.*, **31**, L11109, doi:10.1029/2004GL020225.

Tao, W.-K., 2003: Goddard Cumulus Ensemble (GCE) model: Application for understanding precipitation processes. *Cloud Systems, Hurricanes, and the Tropical Rainfall Measuring Mission (TRMM)*, *Meteor. Monogr.*, No. 51, Amer. Meteor. Soc., 107–138.

——, 2007: Cloud resolving modeling. *J. Meteor. Soc. Japan*, **85B**, 305–330, doi:10.2151/jmsj.85B.305.

——, and S.-T. Soong, 1986: A study of the response of deep tropical clouds to mesoscale processes: Three-dimensional numerical experiments. *J. Atmos. Sci.*, **43**, 2653–2676, doi:10.1175/1520-0469(1986)043<2653:ASOTRO>2.0.CO;2.

——, and J. Simpson, 1989: Modeling study of a tropical squall-type convective line. *J. Atmos. Sci.*, **46**, 177–202, doi:10.1175/1520-0469(1989)046<0177:MSOATS>2.0.CO;2.

——, and ——, 1993: The Goddard Cumulus Ensemble Model. Part I: Model description. *Terr. Atmos. Ocean. Sci.*, **4**, 35–72.

——, and M. Moncrieff, 2009: Multi-scale cloud-system modeling. *Rev. Geophys.*, **47**, RG4002, doi:10.1029/2008RG000276.

——, J. Simpson, and S.-T. Soong, 1987: Statistical properties of a cloud ensemble: A numerical study. *J. Atmos. Sci.*, **44**, 3175–3187, doi:10.1175/1520-0469(1987)044<3175:SPOACE>2.0.CO;2.

——, ——, S. Lang, M. McCumber, R. Adler, and R. Penc, 1990: An algorithm to estimate the heating budget from vertical hydrometeor profiles. *J. Appl. Meteor.*, **29**, 1232–1244, doi:10.1175/1520-0450(1990)029<1232:AATETH>2.0.CO;2.

——, S. Lang, J. Simpson, and R. Adler, 1993: Retrieval algorithms for estimating the vertical profiles of latent heat release: Their applications for TRMM. *J. Meteor. Soc. Japan*, **71**, 685–700.

——, ——, ——, W. S. Olson, D. Johnson, B. Ferrier, C. Kummerow, and R. Adler, 2000: Vertical profiles of latent heat release and their retrieval for TOGA COARE convective systems using a cloud resolving model, SSM/I and ship-borne radar data. *J. Meteor. Soc. Japan*, **78**, 333–355.

——, and Coauthors, 2001: Retrieved vertical profiles of latent heating release using TRMM rainfall products for February 1998. *J. Appl. Meteor.*, **40**, 957–982, doi:10.1175/1520-0450(2001)040<0957:RVPOLH>2.0.CO;2.

——, D. Johnson, C.-L. Shie, and J. Simpson, 2004: Atmospheric energy budget and large-scale precipitation efficiency of convective systems during TOGA COARE, GATE, SCSMEX, and ARM: Cloud-resolving model simulations. *J. Atmos. Sci.*, **61**, 2405–2423, doi:10.1175/1520-0469(2004)061<2405:TAEBAL>2.0.CO;2.

——, and Coauthors, 2006: Retrieval of latent heating from TRMM measurements. *Bull. Amer. Meteor. Soc.*, **87**, 1555–1572, doi:10.1175/BAMS-87-11-1555.

——, S. Lang, X. Zeng, S. Shige, and Y. Takayabu, 2010: Relating convective and stratiform rain to latent heating. *J. Climate*, **23**, 1874–1893, doi:10.1175/2009JCLI3278.1.

Webster, P. J., and R. Lukas, 1992: TOGA-COARE: The Coupled Ocean–Atmosphere Response Experiment. *Bull. Amer. Meteor. Soc.*, **73**, 1377–1416, doi:10.1175/1520-0477(1992)073<1377:TCTCOR>2.0.CO;2.

Wheeler, M. C., and H. H. Hendon, 2004: An all-season real-time multivariate MJO index: Development of an index for monitoring and prediction. *Mon. Wea. Rev.*, **132**, 1917–1932, doi:10.1175/1520-0493(2004)132<1917:AARMMI>2.0.CO;2.

Xie, S., T. Hume, C. Jakob, S. A. Klein, R. B. McCoy, and M. Zhang, 2010: Observed large-scale structures and diabatic heating and drying profiles during TWP-ICE. *J. Climate*, **23**, 57–79, doi:10.1175/2009JCLI3071.1.

Yanai, M., 1961: Dynamical aspects of typhoon formation. *J. Meteor. Soc. Japan*, **39**, 282–309.

——, S. Esbensen, and J.-H. Chu, 1973: Determination of bulk properties of tropical cloud clusters from large-scale heat and moisture budgets. *J. Atmos. Sci.*, **30**, 611–627, doi:10.1175/1520-0469(1973)030<0611:DOBPOT>2.0.CO;2.

Yang, S., and E. A. Smith, 1999a: Moisture budget analysis of TOGA COARE area using SSM/I retrieved latent heating and large-scale Q_2 estimates. *J. Atmos. Oceanic Technol.*, **16**, 633–655, doi:10.1175/1520-0426(1999)016<0633:MBAOTC>2.0.CO;2.

——, and ——, 1999b: Four-dimensional structure of monthly latent heating derived from SSM/I satellite measurements. *J. Climate*, **12**, 1016–1037, doi:10.1175/1520-0442(1999)012<1016:FDSOML>2.0.CO;2.

——, and ——, 2000: Vertical structure and transient behavior of convective–stratiform heating in TOGA COARE from combined satellite–sounding analysis. *J. Appl. Meteor.*, **39**, 1491–1513, doi:10.1175/1520-0450(2000)039<1491:VSATBO>2.0.CO;2.

——, W. S. Olson, J.-J. Wang, T. L. Bell, E. A. Smith, and C. D. Kummerow, 2006: Precipitation and latent heating distributions from satellite passive microwave radiometry. Part II: Evaluation of estimates using independent data. *J. Appl. Meteor.*, **45**, 721–739, doi:10.1175/JAM2370.1.

Yoneyama, K., and Coauthors, 2008: MISMO field experiment in the equatorial Indian Ocean. *Bull. Amer. Meteor. Soc.*, **89**, 1889–1903, doi:10.1175/2008BAMS2519.1.

Yuter, S. E., and R. A. Houze Jr., 1995: Three-dimensional kinematic and microphysical evolution of Florida cumulonimbus. Part II: Frequency distributions of vertical velocity, reflectivity, and differential reflectivity. *Mon. Wea. Rev.*, **123**, 1941–1963, doi:10.1175/1520-0493(1995)123<1941:TDKAME>2.0.CO;2.

——, ——, E. A. Smith, T. T. Wilheit, and E. Zipser, 2005: Physical characterization of tropical oceanic convection observed in KWAJEX. *J. Appl. Meteor.*, **44**, 385–415, doi:10.1175/JAM2206.1.

Zeng, X., and Coauthors, 2007: Evaluating clouds in long-term cloud-resolving model simulations with observational data. *J. Atmos. Sci.*, **64**, 4153–4177, doi:10.1175/2007JAS2170.1.

——, W.-K. Tao, S. Lang, A. Y. Hou, M. Zhang, and J. Simpson, 2008: On the sensitivity of atmospheric ensembles to cloud microphysics in long-term cloud-resolving model simulations. *J. Meteor. Soc. Japan*, **86A**, 45–65, doi:10.2151/jmsj.86A.45.

——, and Coauthors, 2009a: A contribution by ice nuclei to global warming. *Quart. J. Roy. Meteor. Soc.*, **135**, 1614–1629, doi:10.1002/qj.449.

——, and Coauthors, 2009b: An indirect effect of ice nuclei on atmospheric radiation. *J. Atmos. Sci.*, **66**, 41–61, doi:10.1175/2008JAS2778.1.

——, W.-K. Tao, T. Matsui, S. Xie, S. Lang, M. Zhang, D. Starr, and X. Li, 2011: Estimating the ice crystal enhancement factor in the tropics. *J. Atmos. Sci.*, **68**, 1424–1434, doi:10.1175/2011JAS3550.1.

——, ——, S. Powell, R. A. Houze Jr., P. Ciesielski, N. Guy, H. Pierce, and T. Matsui, 2013: A comparison of the water budgets between clouds from AMMA and TWP-ICE. *J. Atmos. Sci.*, **70**, 487–503, doi:10.1175/JAS-D-12-050.1.

Zhang, C., 2005: Madden–Julian oscillation. *Rev. Geophys.*, **43**, RG2003, doi:10.1029/2004RG000158.

——, and S. M. Hagos, 2009: Bi-modal structure and variability of large-scale diabatic heating in the tropics. *J. Atmos. Sci.*, **66**, 3621–3640, doi:10.1175/2009JAS3089.1.

Zhang, G. J., and M. Mu, 2005: Effects of modifications to the Zhang–McFarlane convection parameterization on the simulation of the tropical precipitation in the National Center for Atmospheric Research Community Climate Model, version 3. *J. Geophys. Res.*, **110**, D09109, doi:10.1029/2004JD005617.

——, and X. Song, 2009: Interaction of deep and shallow convection is key to Madden–Julian oscillation simulation. *Geophys. Res. Lett.*, **36**, L09708, doi:10.1029/2009GL037340.

Zhang, M. H., and J. L. Lin, 1997: Constrained variational analysis of sounding data based on column-integrated budgets of mass, moisture, and momentum: Approach and application to ARM measurements. *J. Atmos. Sci.*, **54**, 1503–1524, doi:10.1175/1520-0469(1997)054<1503:CVAOSD>2.0.CO;2.

——, ——, R. T. Cederwall, J. J. Yio, and S. C. Xie, 2001: Objective analysis of ARM IOP data: Method and sensitivity. *Mon. Wea. Rev.*, **129**, 295–311, doi:10.1175/1520-0493(2001)129<0295:OAOAID>2.0.CO;2.

Zipser, E. J., 2003: Some views on ''hot towers'' after 50 years of tropical field programs and two years of TRMM data. *Cloud Systems, Hurricanes and the Tropical Rainfall Measuring Mission (TRMM)—A Tribute to Dr. Joanne Simpson*, *Meteor. Monogr.*, No. 51, Amer. Meteor. Soc., 49–58.

——, R. J. Meitin, and M. A. LeMone, 1981: Mesoscale motion fields associated with a slowly moving GATE convective band. *J. Atmos. Sci.*, **38**, 1725–1750, doi:10.1175/1520-0469(1981)038<1725:MMFAWA>2.0.CO;2.